Cell Stem Cell

Article

ROS Dynamics Delineate Functional States of Hippocampal Neural Stem Cells and Link to Their Activity-Dependent Exit from Quiescence

Graphical Abstract

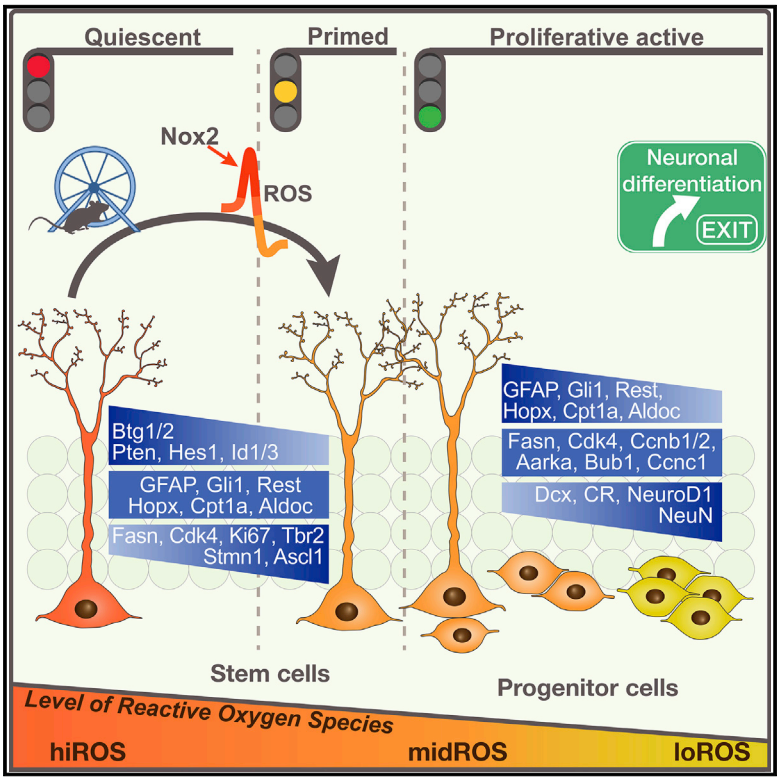

Highlights

- A ROS gradient delineates cell types in the course of adult hippocampal neurogenesis
- Quiescent hippocampal stem cells have unusually high intracellular ROS
- Physical activity recruits quiescent stem cells in a ROS-dependent manner
- NOX2 dependency distinguishes this recruitment from baseline proliferation

Authors

Vijay S. Adusumilli, Tara L. Walker, Rupert W. Overall, ..., Jörg Mansfeld, Annette E. Rünker, Gerd Kempermann

Correspondence

gerd.kempermann@dzne.de

In Brief

Adusumilli et al. show that quiescent stem cells in the adult hippocampus are marked by very high levels of reactive oxygen species (ROS). Physical activity triggers a Nox2-dependent increase and consecutive reduction of intracellular ROS, which recruits stem cells into the cell cycle and thereby increases hippocampal neurogenesis.

Adusumilli et al., 2021, Cell Stem Cell *28*, 300–314
February 4, 2021
https://doi.org/10.1016/j.stem.2020.10.019

CellPress

CellPress
OPEN ACCESS

Cell Stem Cell

Article

ROS Dynamics Delineate Functional States of Hippocampal Neural Stem Cells and Link to Their Activity-Dependent Exit from Quiescence

Vijay S. Adusumilli,[1,2,8] Tara L. Walker,[1,2,7,8] Rupert W. Overall,[1,2,8] Gesa M. Klatt,[1,2] Salma A. Zeidan,[1,2,5] Sara Zocher,[1,2] Dilyana G. Kirova,[4] Konstantinos Ntitsias,[1,2] Tim J. Fischer,[1,2] Alex M. Sykes,[5] Susanne Reinhardt,[3] Andreas Dahl,[3] Jörg Mansfeld,[4,6] Annette E. Rünker,[1,2,9] and Gerd Kempermann[1,2,9,10,*]

[1]German Center for Neurodegenerative Diseases (DZNE) Dresden, Dresden, Germany
[2]Center for Regenerative Therapies Dresden (CRTD), Technische Universität Dresden, Dresden, Germany
[3]DRESDEN-*concept* Genome Center, DFG NGS Competence Center, c/o Center for Molecular and Cellular Bioengineering (CMCB), Technische Universität Dresden, Dresden, Germany
[4]Cell Cycle, Biotechnology Center (Biotec), Technische Universität Dresden, Dresden, Germany
[5]Max Planck Institute for Molecular Cell Biology and Genetics, Dresden, Germany
[6]Institute of Cancer Research, London, UK
[7]Present address: Queensland Brain Institute (QBI), The University of Queensland, Brisbane, Australia
[8]These authors contributed equally
[9]These authors contributed equally
[10]Lead Contact
*Correspondence: gerd.kempermann@dzne.de
https://doi.org/10.1016/j.stem.2020.10.019

SUMMARY

Cellular redox states regulate the balance between stem cell maintenance and activation. Increased levels of intracellular reactive oxygen species (ROS) are linked to proliferation and lineage specification. In contrast to this general principle, we here show that in the hippocampus of adult mice, quiescent neural precursor cells (NPCs) maintain the highest ROS levels (hiROS). Classifying NPCs on the basis of cellular ROS content identified distinct functional states. Shifts in ROS content primed cells for a subsequent state transition, with lower ROS content marking proliferative activity and differentiation. Physical activity, a physiological activator of adult hippocampal neurogenesis, recruited hiROS NPCs into proliferation via a transient Nox2-dependent ROS surge. In the absence of Nox2, baseline neurogenesis was unaffected, but the activity-induced increase in proliferation disappeared. These results provide a metabolic classification of NPC functional states and describe a mechanism linking the modulation of cellular ROS by behavioral cues to the activation of adult NPCs.

INTRODUCTION

The dentate gyrus (DG) of the adult mammalian hippocampus is a unique structure that maintains adult neurogenesis of its principal neurons, the granule cells. The adult-generated neurons provide a particular type of structural plasticity, critical to the function of the DG (Garthe et al., 2009; Sahay et al., 2011). Multi-potent neural precursor cells (NPCs) with elaborate radial glial morphology (referred to as radial-glia like [RGL] or type 1 cells) line the sub-granular zone of the DG and sporadically transition from a quiescent to a proliferation state. They can undergo symmetric self-renewing or asymmetric divisions leading to transient amplifying cells (type 2 cells; intermediate progenitor cells [IPCs]). These IPCs are progressively specified into neuroblasts (NBs; type 3), leading to the generation of adult-born neurons. To sustain this process for extended periods, state transitions of type 1 cells must be tightly controlled.

A hallmark of adult hippocampal neurogenesis is that different regulatory checkpoints are responsive to physiological stimulation such as physical activity and housing in enriched environments (Kempermann et al., 1997; Kronenberg et al., 2003; van Praag et al., 1999). Although many mediating pathways have been described (Jang et al., 2013; Klempin et al., 2013; Lugert et al., 2010), it remains unknown whether subsets of NPCs exist and whether their functional states might be linked to their response to environmental stimuli. We here now demonstrate that cell-autonomous redox regulation is one pathway delineating activatable functional states of adult hippocampal NPCs. A cell's redox status, or cellular "oxidative stress," is generally maintained by a balance between generation and scavenging of reactive oxygen species (ROS) and reactive nitrogen species (RNS). ROS is a product of incomplete reduction of molecular oxygen. Cellular ROS exists primarily as the highly reactive superoxide anion (O^{-}_{2}), which is enzymatically reduced

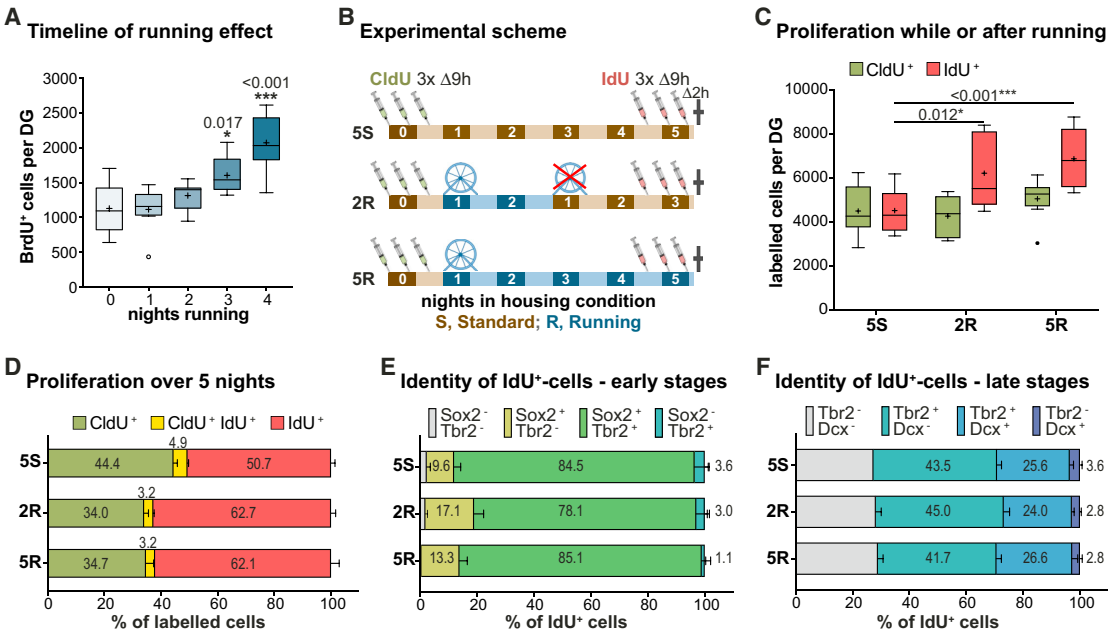

Figure 1. Physical Activity Stimulates Quiescent Cells into an Invariable Proliferation Scheme

(A) Three nights of physical activity are required to significantly increase the number of proliferating ($BrdU^+$) cells in the DG.

(B) Experimental design for the dual thymidine labeling and running paradigm.

(C) Although there is no change in baseline proliferating cells ($CldU^+$), the number of IdU^+ cells significantly increase in the 2R and 5R groups.

(D) The small proportion of $CldU^+IdU^+$ cells indicates that most proliferating cells had exited the cell cycle within the 5 day paradigm.

(E and F) The proportion of the IdU^+ cells that are in early (E) or late (F) stages of the neurogenic trajectory.

The horizontal line in the boxplots indicates the median, and the + sign denotes the mean. Bar plots show mean ± SEM. *$p < 0.05$, **$p < 0.01$, and ***$p < 0.001$. For further details pertaining to replicate numbers, see Table S5.

to hydrogen peroxide (H_2O_2) and hydroxyl radicals ($^{\cdot}OH$) (Bigarella et al., 2014; Holmström and Finkel, 2014; Phaniendra et al., 2015). Sub-cellular compartments such as mitochondria, endoplasmic reticulum, lysosomes, and the plasma membrane can generate cellular ROS as a metabolic by-product or through enzymatic activity of the NADPH oxidizing enzyme (Nox) homologs xanthine oxidase and cyclooxygenase (Ye et al., 2015). The absolute cellular ROS content, and its relative changes, can regulate the abundance of various redox sensors and thus can act as a physiological secondary messenger integrating environmental cues and cell-autonomous signaling. Several lines of work have discussed this role of ROS fluctuations and oxidative stress in regulating stem cell fate in bone marrow cells, cardiac cells, or induced pluripotent stem cells (iPSCs). In those cell types, lower ROS content generally marks quiescence or self-renewal, with a more oxidized state marking cells with higher proliferation rates and lineage commitment (Armstrong et al., 2010; Gurusamy et al., 2009; Smith et al., 2000).

NPCs of the DG and the subventricular zone (SVZ) differ in several aspects, including their susceptibility to become activated by physiological stimuli (Brown et al., 2003). In addition to identifying redox regulation as a key discriminator between adult NPCs of the SVZ and DG niches, we describe the differential enrichment of cellular ROS within functional subsets of NPCs in the adult DG as well as its unexpected specificity in regulating cellular state transitions. We suggest a critical role for cellular ROS dynamics in mediating the activity-dependent recruitment of quiescent hippocampal NPCs into proliferation.

RESULTS

Physical Activity Recruits Non-dividing, Activatable Stem Cells into Proliferation

An extrinsic stimulus such as physical activity might act individually or synergistically, at different neurogenesis checkpoints (Overall et al., 2016). We have previously shown that continuous running wheel access for 4 nights resulted in an increase in the number of proliferating cells in the DG (Overall et al., 2013). We now investigated the dynamics preceding this activation by studying bouts of physical activity of shorter duration (1, 2, 3, or 4 nights; Figure S1A). We found that at least 3 nights of physical activity were required for a significant pro-proliferative response, measured by thymidine analog (BrdU) incorporation into dividing cells (one-way ANOVA: $F_{4,35} = 13.04$, $p < 0.001$; 0 days: 1,130 ± 125 cells versus 3 days: 1,603 ± 93 cells, mean ± SEM, Dunnett: $p = 0.017$; increase of 42%; Figure 1A). At day 4, the proliferative pool had further increased to 183% of control values (4 days: 2,070 ± 142 cells; Dunnett: $p < 0.001$; Figure 1A; see also Akers et al., 2014).

To determine whether the increase in proliferation was driven primarily by an expansion of already dividing cells or by RGL cells exiting quiescence, we applied a dual thymidine analog (CldU, IdU) labeling paradigm (outlined in Figure 1B; Brandt et al., 2012; Fischer et al., 2014; Shibui et al., 1989) and housed animals either with access to a running wheel (5R) or in standard housing conditions (5S) for a period of 5 nights (i.e., 4 full days). To also detect the effect of an acute bout of physical

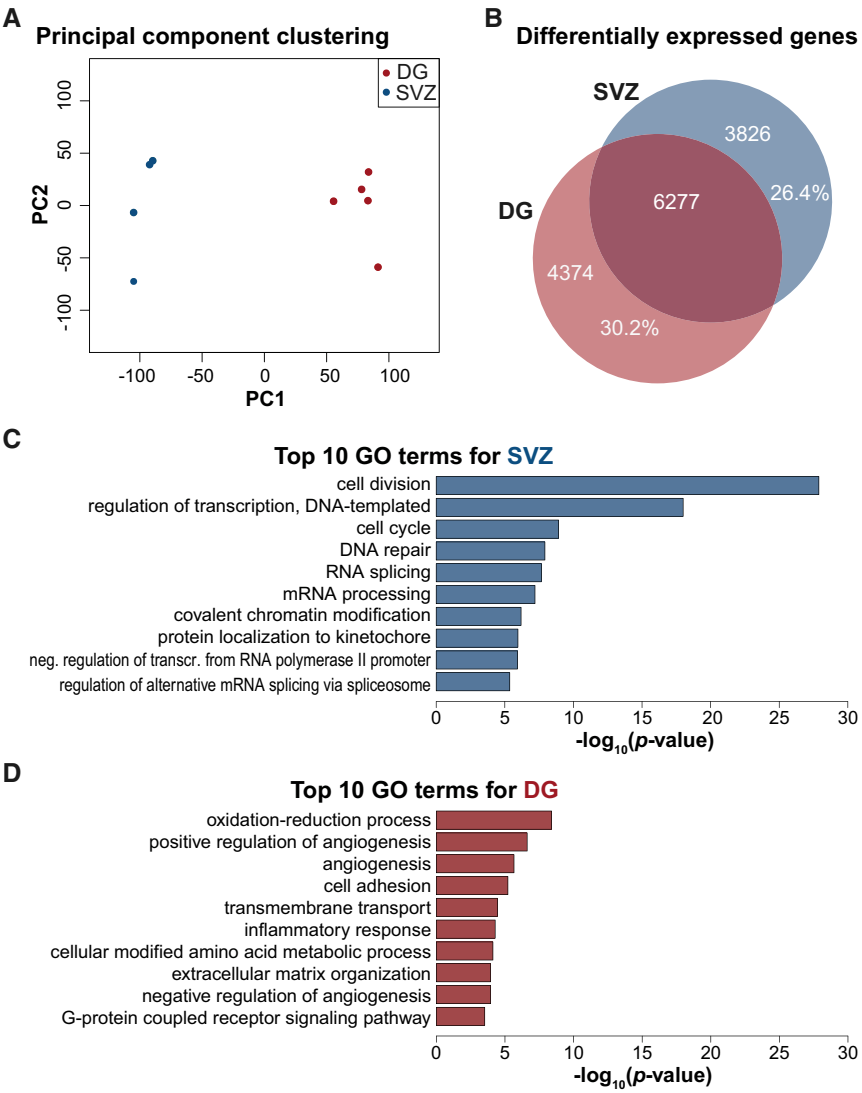

Figure 2. Nes-GFP$^+$ Cells of the DG and SVZ Can Be Distinguished on the Basis of Their Differential Regulation of ROS

(A) A principal-component analysis showed that Nes-GFP$^+$ samples from DG and SVZ cluster distinctly.

(B) About 30% and ~26% of the detected transcripts are uniquely expressed in the NPCs of the DG and SVZ respectively ("signatures").

(C) A Gene Ontology (GO) analysis of the signatures revealed that the most enriched pathways in the SVZ precursor cells were related to cell division and transcriptional regulation.

(D) In contrast, redox regulation was identified as the most enriched pathway in the DG.

activity, a third group of mice had running wheel access only for 2 nights (2R) before returning to standard conditions for the remaining 3 nights. On the basis of the number of IdU$^+$ cells, we found a strong pro-proliferative response in the 5R group (6,876 ± 474; increase of 52%; two-way ANOVA, n = 8: interaction: $p = 0.046$, $F_{2,42} = 3.33$, Dunnett: $p < 0.001$; Figure 1C). Interestingly, an increase in the number of IdU$^+$ cells was also seen in the 2R group (6,217 ± 581, increase of 38%, $p = 0.01$), not only confirming the hypothesis of the acute nature of the stimulus but also suggesting that physical activity represents rather an activation event. In contrast, no significant differences were detected in the numbers of CldU$^+$ cells across the three groups (5S: 4,496 ± 398; 2R: 4,265 ± 319, $p = 0.896$; 5R: 5,052 ± 328, $p = 0.547$), suggesting no effect of *de novo* activity on proliferating cells' survival within the experimental time frame. We noted that only a small proportion of CldU$^+$ cells were positive for IdU (5S: 10.0% ± 0.9%; 2R: 8.7% ± 1.0%; 5R: 8.5% ± 0.4%; Figure 1D shows percentages of all labeled cells), suggesting that the majority of NPCs exit the cell cycle within the experimental time frame irrespective of activity stimulus.

To determine whether the CldU$^-$IdU$^+$ cells activated by physical activity would predominantly expand the NPC stage, or instead progress to advanced stages of adult neurogenesis as do the cells proliferating in the absence of a run stimulus (Kronenberg et al., 2003), we phenotyped cells using two different sets of antibodies to identify type 1 and type 2 cells (Sox2/Tbr2; potentially also including rare dividing astrocytes; "early"; Figure 1E) or type 2b and type 3 cells (Tbr2/Dcx; "late"; Figure 1F). Under standard housing conditions, the majority of IdU$^+$ cells (84.5% ± 4.9%) were double-positive for Sox2 and Tbr2, whereas 9.6% ± 2.4% were exclusively positive for Sox2 and 3.6% ± 1.6% showed only Dcx expression. Stimulation by physical activity (5R or 2R) did not significantly alter these proportions. Furthermore, phenotyping CldU$^+$ cells did not yield any significant changes between animals in different housing conditions (Figures S1D and S1E). These results suggest that physical activity stimulates a population of quiescent, yet activatable NPCs to enter proliferation without otherwise affecting the survival and the distribution among the neurogenic stages.

Enrichment of Redox Regulation Transcriptionally Delineates Subsets of Precursor Cells within DG and SVZ

As SVZ cells do not show a neurogenic response to exercise (Figures S1B and S1C; Brown et al., 2003), we hypothesized that a direct comparison of expression profiles might reveal differentially enriched pathways, which potentially maintain a distinct population of activatable NPCs in the DG. To identify such pathways, we compared the transcriptomic profiles of reporter-marked NPCs (Nes-GFP$^+$; Yamaguchi et al., 2000) from the DG with those from the SVZ, isolated from the same standard-housed animals.

A principal-component analysis (PCA) showed that Nes-GFP$^+$ cells from the two niches clustered distinctly (Figure 2A; Figures

S1F–S1H), with 30.2% of all transcripts uniquely enriched within the DG and 26.4% of all transcripts unique to the SVZ ("signatures"; Figure 2B). A Gene Ontology (GO) enrichment analysis showed that the top enriched pathways in the SVZ were related to "cell division," "transcriptional regulation," and "cell cycle" (Figure 2C; see also Table S1). The enriched pathways of the DG, in contrast, were related to cellular responses to environmental modulations, and of these, "redox regulation" showed the greatest enrichment ($p = 4 \times 10^{-9}$; Figure 2D; see also Table S1).

To validate whether ROS levels, and thus the redox state, are differentially maintained and regulated in the DG compared with the SVZ, we stained dissociated cells from both niches for total cellular ROS using the superoxide indicator dihydroethidium (DHE; Dikalov and Harrison, 2014; Zhou et al., 2016; Zielonka et al., 2008). We discovered that DG (Figures 3A–3D) and SVZ (Figures 3E–3H) cells isolated from the same animals had distinct ROS profiles (Figures 3A, 3E, and 3I; gating strategy: Figures S2A–S2D). The SVZ cells had significantly higher overall ROS levels than the DG cells (two-way ANOVA, interaction: $p < 0.001$, $F_{1,16} = 32.85$; Tukey, $p = 0.005$; Figure 3I, left; compare also dotted lines in Figures 3C and 3G; validated using different ROS dyes). We used the neurosphere (NS) bioassay to determine whether the cell-intrinsic ROS content of DG cells could predict their *in vitro* stemness (Reynolds and Weiss, 1992; Rietze and Reynolds, 2006). Indeed, 98.8% NSs were generated from the 17.8% ± 1.1% of fluorescence-activated cell sorting (FACS) events with the highest ROS content (Figure S2F). This corresponds to an 8.2 ± 1.5-fold ROS-associated enrichment of NS-forming cells relative to unsorted cells (one-sample t test, $p = 0.008$).

To further resolve the correlation between ROS content and the potential for NS formation, we defined four distinct, non-overlapping classes of ROS levels (Figures 3A–3C): hiROS (2.1% ± 0.3% events with highest ROS levels), midROS (next 9.5% ± 1.5% events), loROS (next 38.6% ± 4.7% events), and noROS (48.9% ± 5.8% events; Figure 3B). In the SVZ (Figures 3E–3G), we found that most cells were in the loROS (62.0% ± 6.2%) and midROS (25.7% ± 4.7%) classes, with substantially fewer in the hiROS class (0.3% ± 0.0%). From both the SVZ and DG, NS-forming cells were restricted to the higher ROS classes (midROS and hiROS classes, which together constitute 26% and 11.6% of all sorted events from the SVZ and DG, respectively), with the highest density of NS-forming cells in the hiROS class compared with unstained, sorted cells (DG: 9.7 ± 1.0-fold relative to unstained, SVZ: 14.2 ± 2.0-fold; one-sample t tests with false discovery rate [FDR] correction, DG: $p_{adj} = 0.002$, SVZ: $p_{adj} = 0.015$; Figures 3D and 3H). Supplementing the growth medium with KCl or norepinephrine (NE), treatments that can boost NS formation from DG precursors (Jhaveri et al., 2010; Walker et al., 2008), augmented NS formation from hiROS and midROS cells, with more NSs induced in the hiROS class after KCl treatment (2.4 ± 0.7-fold; two-way ANOVA, interaction: $p = 0.003$, $F_{6,36} = 4.15$; Dunnett: $p < 0.001$; Figure S2G). Neither KCl nor NE elicited NS formation from loROS and noROS classes. On the basis of these results and those of others (Le Belle et al., 2011), we conclude that cellular ROS content is an effective predictor of NS-forming potential and that the stemness of adult NPCs is related to their steady-state cellular ROS content.

Although we found that the ROS content of Nes-GFP$^+$ cells of the DG was much greater than that of all isolated cells (3.7-fold; Tukey, $p = 0.001$; Figure 3I), a disproportionate concentration of Nes-GFP$^+$ precursor cells in the higher ROS classes alone does not explain the finding that these classes exclusively harbor the NS-forming cells. Analyzing the distribution of Nes-GFP$^+$ cells of the DG into the four ROS classes (Figure 3J; gating: Figures S2A–S2E) revealed the following characteristic pattern: 50% of the Nes-GFP$^+$ cells were negative for or low in ROS (noROS: 5.3% ± 3.9% of all Nes-GFP$^+$ cells; loROS: 50.8% ± 3.7%), representing sub-populations that are not competent to form NSs. An additional 24.5% ± 5.1% of Nes-GFP$^+$ cells localized to the midROS and 19.4% ± 7.4% to the hiROS class (Figure 3L). In contrast, the Nes-GFP$^+$ cells of the SVZ had lower absolute ROS levels than all isolated cells (Tukey, $p = 0.015$; Figure 3I) with, compared with the DG, more precursor cells in the noROS class (35.3% ± 3.9%; two-way ANOVA, interaction: $p < 0.001$, $F_{3,32} = 13.0$; Sidak, $p < 0.001$; Figure 3K), and fewer (1.22% ± 0.4%, $p = 0.015$) in the hiROS class (Figures 3K–3M).

These results suggest that (1) NPCs of the DG are maintained at a higher cellular ROS content compared with the surrounding other DG cells; (2) cellular ROS content resolves the precursor pools of DG and SVZ into distinct functional classes with different stemness potential *ex vivo*; and (3) compared with the SVZ, the Nes-GFP$^+$ hiROS population is substantially enriched in the DG.

Nes-GFP$^+$ Cells of the Different ROS Classes Have Distinct Molecular Profiles

To verify if ROS-based clustering identifies cell populations with truly distinct functional states, we sequenced RNA from Nes-GFP$^+$ cells of the DG sorted by ROS class. As only a very small proportion of Nes-GFP$^+$ cells fell into the noROS fraction (5.26% ± 3.87%), we omitted this group from the following analysis. The Nes-GFP$^+$ cells in each ROS class had distinct transcription profiles, as shown by PCA (PC1: 41% and PC2: 13%; Figure 4A; see also Figures S3A–S3C). We found that 47.7% of expressed transcripts segregated on the basis of ROS content, with 36.1% of transcripts specific to cells of only one ROS class. We identified 12.1% of all expressed transcripts specific for the hiROS class (hiROS signatures), 6.9% for midROS, and 17.1% for loROS (Figure 4B; see also Table S2). Additionally, 4.5% of all the transcripts were co-enriched between the hiROS and midROS classes and 6.9% between midROS and loROS. Only 25 transcripts (0.2%) were in both hiROS and loROS, confirming these classes to be the most distinct. We compared these profiles to the transcriptome data from the SVZ and DG (Figure 2). Transcripts found in DG Nes-GFP$^+$ cells, compared with the SVZ, showed highest enrichment in the hiROS signatures, and conversely, the SVZ-specific transcripts showed higher enrichment for loROS signatures (Figure 4C). This strongly suggests that the hiROS population is unique to the DG.

To further resolve this heterogeneity, we investigated the expression of transcripts known to mark cellular processes such as neurogenesis, cell cycle, and, as a control, ROS regulation (see Table S3). With decreasing cellular ROS content, expression of transcripts essential for maintenance of cellular

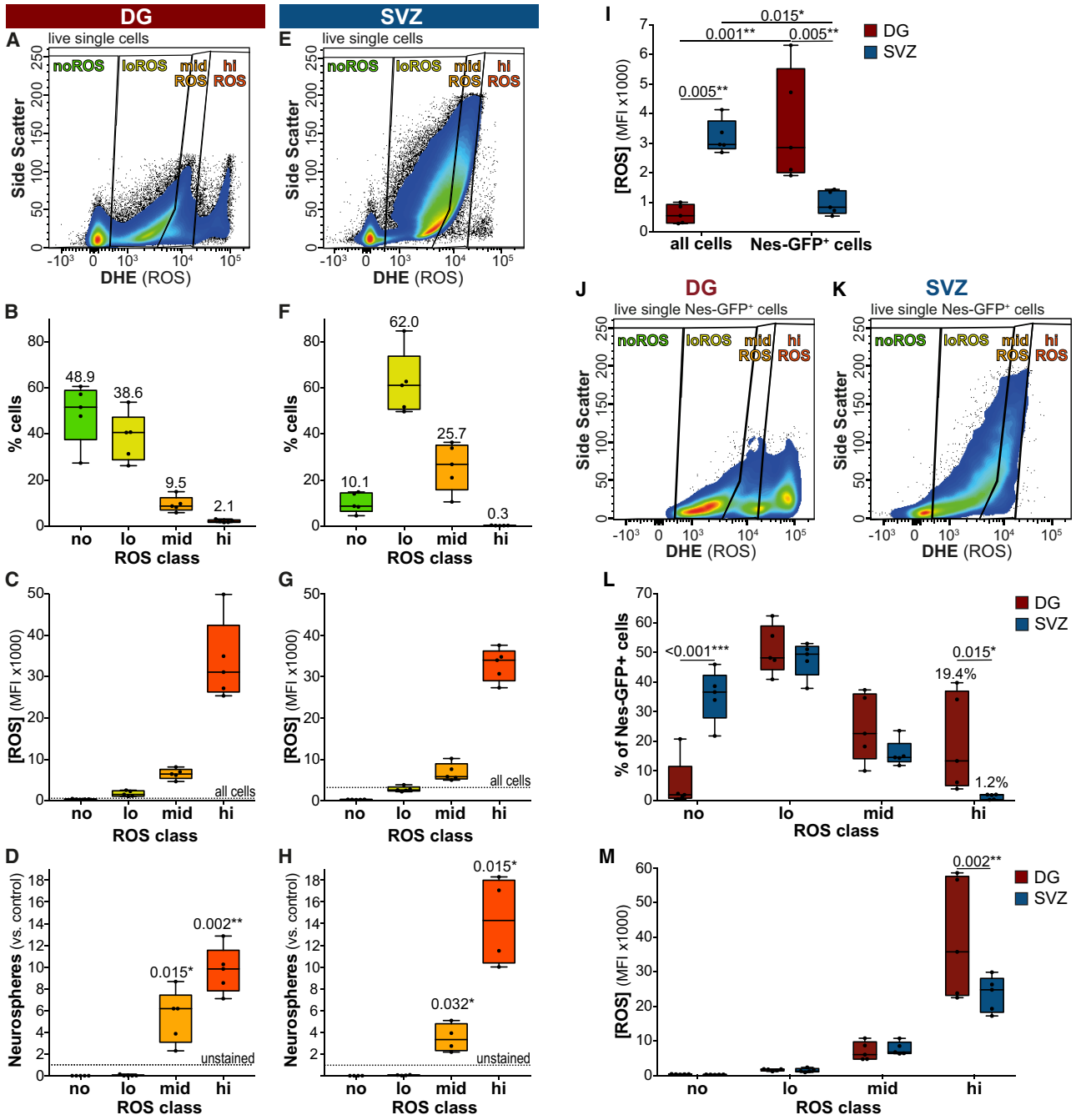

Figure 3. Nes-GFP$^+$ Cells Can Be Classified into Distinct Functional Subsets on the Basis of Their Cellular ROS Content

(A and E) Flow cytometry revealed that cells from the DG (A) and SVZ (E) have distinct ROS profiles (see Figures S2A–S2E for gating strategy).

(B, C, F, and G) Plots showing the distribution (B and F) and cellular ROS content (C and G) of cells in each of the four manually gated ROS classes.

(D and H) NS formation is restricted to the midROS and hiROS classes, with more neurospheres formed from hiROS cells from both the DG (D) and SVZ (H).

(I) The ROS content in SVZ cells is higher than in DG cells (all cells). Nes-GFP$^+$ cells of the DG have higher ROS than those of the SVZ.

(J and K) Gating of Nes-GFP$^+$ cells from the DG (J) and SVZ (K) on the basis of ROS content.

(L) The DG and SVZ show unique distribution patterns across the four ROS classes, with more cells from the DG in the hiROS class.

(M) The Nes-GFP$^+$ cells from the DG have higher levels of cellular ROS than those from the SVZ.

The horizontal line within the boxplots indicates the median and the + sign denotes the mean. *$p < 0.05$, **$p < 0.01$, and ****$p < 0.001$.

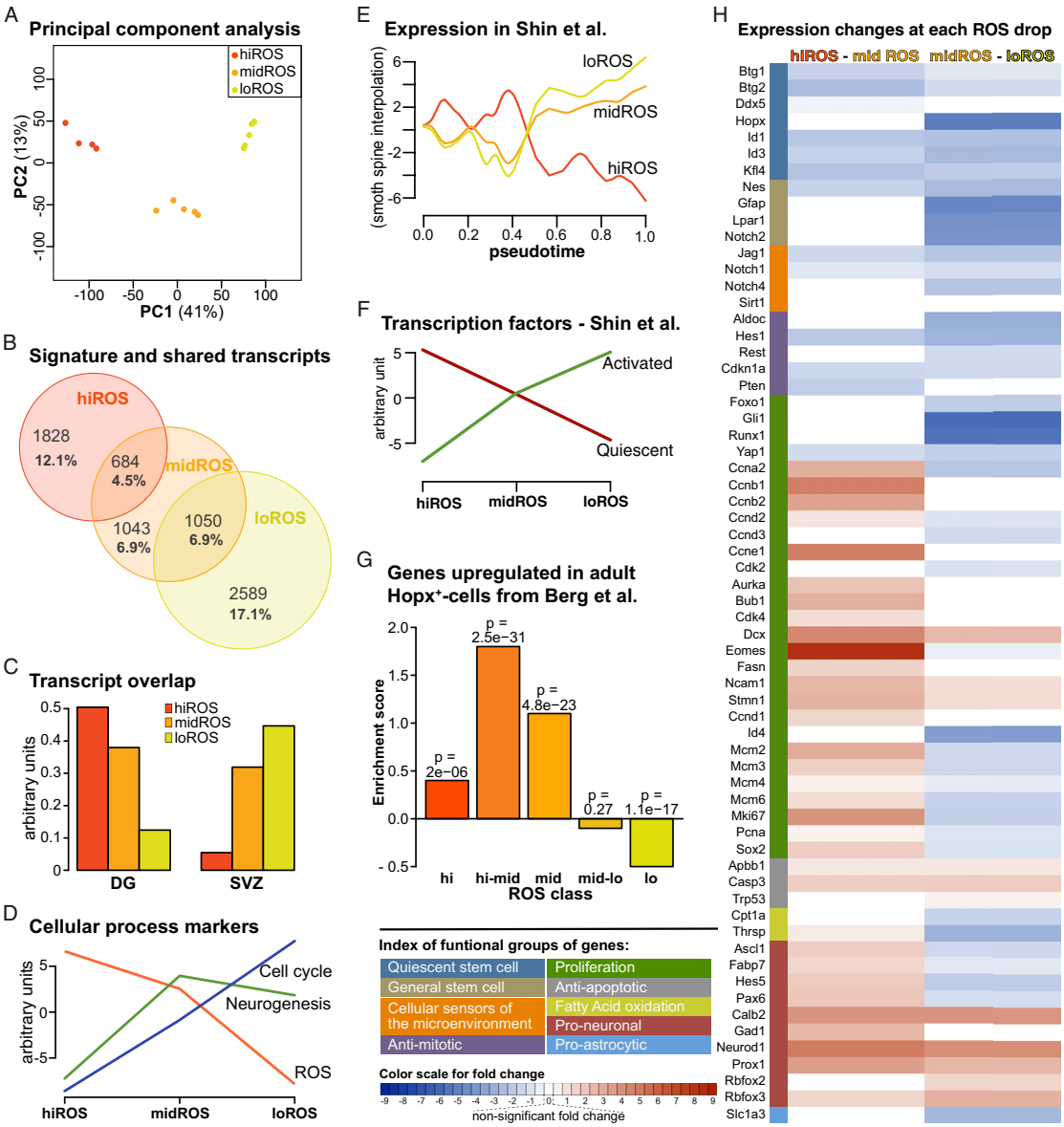

Figure 4. ROS Levels Decrease along the Neurogenic Trajectory

(A) PCA shows that the different ROS groups have distinct transcriptional profiles.

(B) Venn diagram showing similarities in gene expression between the different ROS classes. Note that the 0.2% transcripts co-enriched in hiROS and loROS are omitted in this panel.

(C) Transcripts upregulated in the DG were enriched in hiROS cells, whereas loROS transcripts showed more overlap with the SVZ signature.

(D) With decreasing ROS, expression of ROS-related genes decreased, while cell cycle activity and neural differentiation genes increased.

(E) In the pseudotime trajectory of Shin et al. (2015), hiROS signature transcripts peaked early, with later peaks in expression for the lower ROS groups.

(F) Decreasing ROS content is associated with increased expression of transcription factors associated with activated stem cells (as identified by Shin et al., 2015) as well as a decrease in expression of quiescent stem cell transcription factors.

(G) Genes upregulated in adult Hopx^{+} cells (Berg et al., 2019) showed enrichment for hiROS and midROS signatures and genes co-expressed in hiROS and midROS.

(H) Heatmap showing expression changes of selected genes at the hiROS to midROS transition (left) and midROS to loROS transition (right).

ROS levels declined, while markers of active cell cycle and neurogenic commitment increased (Figure 4D).

Both hiROS and midROS cells expressed RGL markers such as *Nestin*, *Gfap*, *Notch2*, *Lpar1*, and *Lfng* (Semerci et al., 2017; Walker et al., 2016). There was no detectable expression of *Eomes*, an IPC marker (Tbr2; Hodge et al., 2012); *E2f1*, a potent cell cycle regulator (Black et al., 2005; Cooper-Kuhn et al., 2002); or enrichment for proliferation markers (*Pcna*, *Mki67*, MCMs, and others) in the profiles of the hiROS class. These cells were also marked by weak to no expression of markers of advanced

stages of neurogenesis such as *Dcx*, *Prox1*, *Neurod1*, *Calb2* (Calretinin), and *Rbfox3* (NeuN). The expression of cell cycle inhibitors *Cdkn1a* (Pechnick et al., 2008) and *Pten* (Bonaguidi et al., 2011; Hill and Wu, 2009), critical in controlling proliferation and cell cycle entry of stem cells, was also highest in the hiROS class. Taken together, this expression profile indicated that high ROS marks early-stage quiescent NPCs. Genes reflecting the ability of precursor cells to enter proliferation, such as *Gli1*, *Id4* (Bedford et al., 2005; Boareto et al., 2017), *Yap1*, *Runx1*, and *Foxo1*, were highest in both the hiROS and midROS classes.

The midROS class showed a complex transcript profile. On one hand, similar to hiROS, cells in the midROS class were characterized by expression of genes such as *Rest* (Gao et al., 2011), *Hes1* (Hatakeyama et al., 2004), *Aldoc* (Shin et al., 2015) and *Hopx* (Berg et al., 2019; Shin et al., 2015), which are negatively associated with cell cycle entry. Furthermore, *Thrsp* (Spot14; Knobloch et al., 2014) and *Cpt1a* (Knobloch et al., 2017), components of the fatty acid oxidation (FAO) pathway critical for quiescence exit, were uniquely enriched in the midROS class. Additionally, this class was characterized by the strongest expression of proliferation markers such as *Pcna*, *Mki67*, and Mcm2/3/4/6. We detected cyclins/CDKs required for G1/S transition, such as *E2f1*, Ccnd2/3, *Ccne1*, *Cdk2*, *Ccna2*, and Ccnb1/2, as well as cell cycle promoters *Bub1* and *Aurka*. The midROS cells also had the highest levels of *Sox1*, *Sox2*, and *Sox9* and expressed both pro-neural and astrocytic lineage genes such as *Ascl1* (Andersen et al., 2014; Kim et al., 2011), *Hes5* (Lugert et al., 2010), *Pax6*, and *Fabp7* (BLBP; Codega et al., 2014; Doetsch, 2003) highlighting that these cells are actively engaged in, or poised for, the growth phase of the cell cycle. Genes such as *Dcx*, *Stmn1*, *Fasn* (Knobloch et al., 2013), *Eomes* (Tbr2), *Cdk4*, and *Ncam1*, associated with proliferating neuronally committed cells, were co-enriched in cells of both the midROS and loROS classes. These results indicate that NPCs with moderate ROS levels comprise a mix of cellular states at different stages of neurogenic progression.

The Nes-GFP$^+$ cells of the loROS class were uniquely enriched for transcripts marking neuronal differentiation, including advanced stages such as *Calb2*, *Rbfox3*, *Rbfox2*, *Prox1*, *Neurod1*, and *Gad1*. The loROS class was also enriched for anti-apoptotic and DNA damage checkpoint markers such as *Trp53* (p53), *Casp3*, and *Apbb1*. Taken together, these results suggest that Nes-GFP$^+$ cells with reduced ROS content are committed to neuronal differentiation (Figure S3D).

To corroborate that the ROS classes indeed represent a trajectory from quiescence to neuronal commitment, we investigated the expression of their signature transcripts along the pseudotime trajectory derived from single cell transcriptomic data of Nes-CFP^{nuc} cells by Shin et al. (2015). The hiROS signatures were expressed early in pseudotime, whereas loROS and midROS genes were expressed more strongly later in the reconstructed trajectory (Figure 4E). We further analyzed expression of 82 transcription factors (TFs), attributed by Shin et al. (2015) to either the quiescent or the active proliferative states, in our three ROS classes. We found a clear similarity between TFs regulating quiescence and hiROS signature TFs, a relationship that inverts with the drop in ROS content (Figure 4F). Conversely, TFs associated with active proliferation were almost absent in hiROS cells but increased expression in cells with lower ROS content.

In summary, these findings confirm that hiROS cells correspond to the quiescent stem cell population of the adult DG.

Shifts in Cellular ROS Levels Delineate Distinct Functional States

There is a substantial drop in cellular ROS content between the hiROS and midROS classes (~6-fold reduction; Figure 3M). According to our transcriptional profiling, however, this "ROS drop" does not coincide with changes of known key genes that would mark exit from quiescence, such as *Hopx* (Figure S3E). In order to align changes in cellular ROS content with cellular state transitions, we compared our results to the transcriptomic analysis of adult Hopx$^+$ cells performed by Berg et al. (2019). In that study, the authors identified a gradual shift in expression profiles of Hopx$^+$ NPCs from embryonic to adulthood (P45) and a progressive upregulation of transcripts associated with quiescence. We found that the signature transcripts of Hopx$^+$ cells from the adult DG were significantly under-represented among loROS signature transcripts. The adult Hopx-specific transcripts were not specific to either of the higher ROS classes but showed a strong enrichment in the signature genes and the co-enriched gene sets of the hiROS and midROS classes (Figure 4G), which suggested that several functional states can be resolved within the broader Hopx$^+$ population of NPCs by assessing cellular ROS levels. This meta-analysis, while confirming our initial assertion that the hiROS cells represent quiescent NPCs, prompted us to hypothesize that changes in cellular ROS content precede the exit from quiescence.

To test this hypothesis, we performed a separate comparison of the hiROS versus midROS expression profiles (see STAR Methods) and noticed that the expression of multiple RGL markers (*Gfap*, *Egfr*, *Gli1*, *Lfng*) and genes known to negatively correlate with or regulate proliferation, such as *Id4*, *Aldoc*, *Rest*, *Thrsp*, and *Cpt1a*, was unchanged as the ROS content significantly dropped (Figure 4H; see Table S4 for complete gene list and GO terms associated with the ROS shift). However, we saw a downregulation of cell cycle inhibitors (*Pten*, *Btg1/2*, *Hes1*, *Cdkn1a*, *Klf4*, *Ddx5*) and an upregulation of markers of active proliferation (*Sox2*, *Eomes*, *E2f1*, *Pcna*, *Fasn*, *Dcx*, *Stmn1*, *Hes5*, *Fabp7*, *Prox1*, *Ccnd1/2*, *Cdk4*, *Sirt2*). These results, along with analysis of changes in signature transcripts of adult Hopx$^+$ NPCs (Figure S3F), suggested that although the ROS transition is associated with expression of key genes necessary for quiescence exit, this switch in ROS content precedes the downregulation of other genes maintaining the quiescent state.

A second drop in ROS levels (~2-fold) occurred between the two putative proliferative classes, midROS and loROS, and was marked by decreases in RGL markers (*Gfap*, *Egfr*, *Nes*, *Slc1a3*, *Prom1*, *Notch2*, *Lpar1*), proliferation markers (*Sox2*, *Eomes*, *Pcna*, *Mki67*, *Mcm2/3/4/6*, *Hes5*, *Pax6*), and astrocytic markers (*Fabp7*). Quiescent markers (*Hopx*, *Cpt1a*, *Thrsp*, *Aldoc*) were also strongly downregulated, while *Stmn1* was upregulated together with redox sensors such as *Foxo3* and *Trp53* (Figure 4H). The shift in ROS content from moderate to lower levels is further marked by an increase in markers of neuronal commitment (*Rbfox2/3*, *Neurod1*, *Ncam1*, *Prox1*, *Calb2*) accompanying the cellular progression from transient amplification to a NB-like identity.

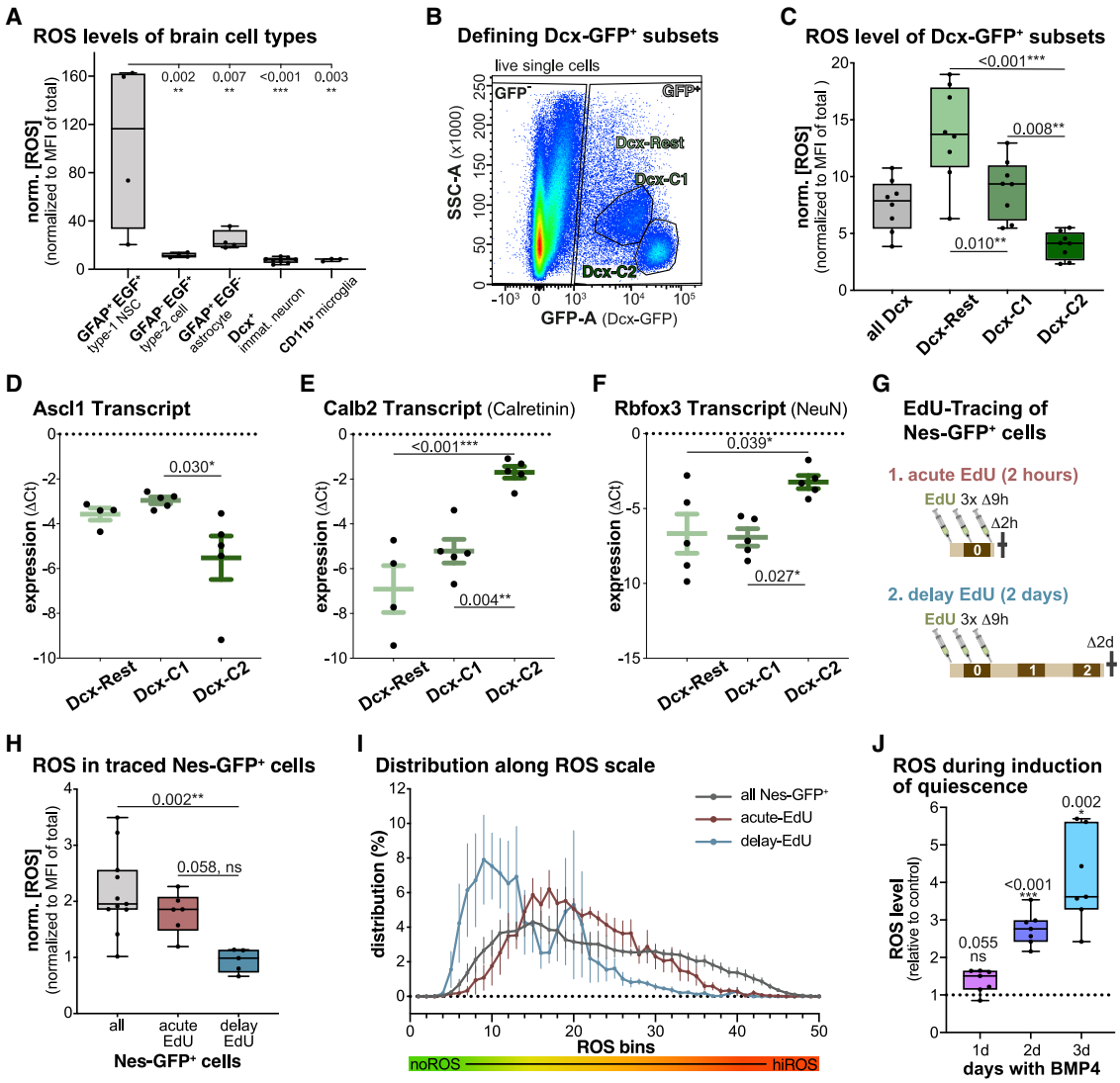

Figure 5. ROS Levels in Different Neurogenic DG Cell Types and *In Vitro* Monolayer Culture

(A) Relative cellular ROS content in major cell types within the DG (see also Figures S4A–S4D).

(B) FACS gating for Dcx-GFP$^+$ sub-clusters.

(C) Cellular ROS content in Dcx-GFP$^+$ sub-clusters (see also Figures S4E and S4F).

(D–F) Relative expression levels of *Ascl1* (D), *Calb2* (E), and *Rbfox3* (F) in the different Dcx-GFP$^+$ subsets normalized to the expression levels of *Actb*.

(G) EdU labeling scheme for assaying cellular ROS content in proliferating cells *in vivo*.

(H) Relative cellular ROS content in Nes-GFP$^+$ cells and the subset of Nes-GFP$^+$EdU$^+$ cells.

(I) Pseudohistogram of Nes-GFP$^+$ cells and their EdU subsets. Each bin contains 2% of all cells.

(J) Relative cellular ROS content in monolayer culture following BMP4 treatment.

For boxplots, the horizontal line indicates the median. Other data represent mean ± SEM.

hiROS NPCs Are Quiescent

Our next experiment(s) aimed to confirm that the quiescent hiROS cells correspond to the type 1 or RGL cells (Kempermann et al., 2004; Gebara et al., 2016). As Nestin has a broad range of expression among DG NPCs, we used combinations of additional reporter lines and markers to profile RGL cells, IPCs, NBs, and microglia of the adult DG (Nolte et al., 2001; Sellgren et al., 2017; Walker et al., 2007). We confirmed that putative RGL cells (Gfap-GFP$^+$EGF$^+$; Nolte et al., 2001) have significantly higher ROS content compared with all other studied cell types (two-way ANOVA, $p < 0.001$, $F_{6,32} = 11.65$; Figures 5A and S4A–S4D). In contrast to Nes-GFP$^+$ cells (Figure 3L; DG), fewer Gfap-GFP$^+$EGF$^+$ cells segregated into the loROS class (20.4% ± 7.0%), and the remaining putative RGL cells distributed equally into the hiROS (37.73% ± 10.44%) and midROS (40.4% ± 4.3%; Figure S4A) classes.

We identified two distinct Dcx-GFP$^+$ cell clusters: Dcx-C1 (42.0% ± 2.8% of all GFP$^+$ cells) and Dcx-C2 (36.0% ± 2.3%; lowest granularity, highest GFP levels; Figure 5B). We grouped cells outside these clusters as Dcx-Rest (16.8% ± 1.7% of all

GFP$^+$ cells; Figure S4E). The Dcx sub-populations differed in cellular ROS content (one-way ANOVA, $F_{2,21}$ = 22.16, p < 0.001; Tukey; Figure 5C), with cells of Dcx-Rest having the highest relative ROS levels (3.5-fold of Dcx-C2, 1.5-fold of Dcx-C1) and cells of Dcx-C2 the lowest (the difference between Dcx-C2 and Dcx-C1 is 2.3-fold). In line with this, cells of the Dcx-C1 and Dcx-C2 clusters segregated predominantly into the loROS class (65.4% ± 8.1% or 88.2% ± 2.2%, respectively), with barely any cells in the hiROS class (C1: 1.5% ± 0.7%, C2: 0.1% ± 0.0%), while Dcx-Rest cells were still present in hiROS (10.1% ± 3.7%; Figure S4F). We found that the Dcx-Rest and Dcx-C1 populations had higher levels of *Ascl1* compared with Dcx-C2 cells (one-way ANOVA, $F_{2,11}$ = 4.85, p = 0.031; Tukey; Figure 5D), indicating a state of transient amplification. On the other hand, Dcx-C2 cells had higher expression of *Calb2* (one-way ANOVA, $F_{2,11}$ = 17.82, p < 0.001; Tukey; Figure 5E) and *Rbfox3* (one-way ANOVA, $F_{2,12}$ = 5.67, p = 0.019; Tukey; Figure 5F) indicating that the Dcx-GFP$^+$ cells with the lowest cellular ROS levels were late-stage NBs (type 3 cells) or post-mitotic immature neurons (see Kempermann et al., 2004).

To further validate that hiROS cells are quiescent, we EdU-labeled (Buck et al., 2008; Zeng et al., 2010) proliferating cells in Nes-GFP animals (Figure 5G) and analyzed tissue after 2 h (acute-EdU$^+$) or 2 days (delayed-EdU$^+$). Compared with the Nes-GFP$^+$ population, cellular ROS levels were similar in the Nes-GFP$^+$ acute-EdU$^+$ cells (one-way ANOVA, $F_{2,19}$ = 7.85, p = 0.003; Tukey, p = 0.428; Figure 5H) and reduced in the Nes-GFP$^+$ delayed-EdU$^+$ cells (p = 0.002). Resolving cells according to their ROS content into 50 bins from low to high ROS (Figure 5I) showed that the Nes-GFP$^+$ cells with higher cellular ROS content were rarely marked by EdU incorporation (see bins 40–50), and an increase in frequency of proliferating Nes-GFP$^+$ cells (Nes-GFP$^+$ acute-EdU$^+$) was concomitant with a ROS shift to moderate levels (wide peak from bin ~12 to 30). Furthermore, cells that were in cell cycle 2 days prior to assay (Nes-GFP$^+$ delayed-EdU$^+$) exhibited much lower ROS levels (major peak around bin 10; Figure 5I).

To address the possibility that our *ex vivo* cytometric protocols induce acute stress that might be associated with non-specific changes in ROS, we exposed proliferating, homogeneous monolayer cultures of DG-derived NPCs (Babu et al., 2007, 2011) to exogenous bone morphogenic protein (BMP4; Knobloch et al., 2017; Martynoga et al., 2013). The BMP4 protocol drives proliferating NPCs into a stable quiescent state without inducing significant cell death (Armenteros et al., 2018; Martynoga et al., 2013). Three days of BMP4 treatment induced a marked change in cellular morphology, and no proliferating cells were detectable by EdU incorporation (3 h chase; Figure S4G). This transition from proliferation to quiescence was accompanied by a progressive and significant increase in cellular ROS levels (relative to the proliferating control; 2 days: 2.8 ± 0.2-fold; 3 days: 4.09 ± 0.46-fold; one-sample t test 1 day: t_6 = 3.2, 2 days: t_6 = 10.5, 3 days: t_6 = 6.7; FDR correction; Figure 5J).

Transient Delineated ROS Fluctuations Are Observed in Nes-GFP$^+$ Cells in Response to Physical Activity

Having established that the hiROS cells correspond to a quiescent NPC population, and that a drop in ROS levels precedes exit from quiescence, we next sought to link these data to our initial observation that the acute physical activity involves recruitment of quiescent cells into proliferation. We thus subjected Nes-GFP reporter mice to two physical activity paradigms: first, an acute bout of 1 single night of wheel access, not sufficient to elicit a measurable increase in proliferation (compare Figure 1A), and second, 4 nights of wheel access, which elicits a proliferative response. Analyzing the NPC-ROS profiles under these conditions, we found that after 1 night of running, the distribution of Nes-GFP$^+$ cells among ROS classes was not different from control conditions (Figure 6A). However, there was a robust additional surge in the cellular ROS content exclusively in the Nes-GFP$^+$ cells of the hiROS class (increase to 152.6% ± 25.3%; two-way ANOVA, interaction p = 0.021, $F_{6,64}$ = 2.70; Tukey: hiROS Std versus 1dRun, p = 0.001; Figure 6B). Although this spike in cellular ROS content in hiROS NPCs returned to control levels after 4 nights of physical activity (Tukey: Std versus 4dRun, p = 0.44; 1dRun versus 4dRun, p < 0.001; Figure 6B), we observed a redistribution of Nes-GFP$^+$ cells to the different ROS classes at this time point. Compared with standard-housed controls, we detected an increase by a third (from 50.8% to 67.2% of all Nes-GFP$^+$ cells) in the proportion of Nes-GFP$^+$ cells in the proliferative and neuronally committed loROS class (two-way ANOVA, interaction: p = 0.046, $F_{6,64}$ = 2.29; Tukey, loROS: Std versus 4dRun: p = 0.034, 1dRun versus 4dRun: p = 0.020; Figure 6A).

For comparison, in the SVZ, the Nes-GFP$^+$ cells of the hiROS class showed a similar ROS spike (two-way ANOVA, interaction: ns, housing: p = 0.045, $F_{1,32}$ = 4.37; Sidak, loROS: p = 0.005; Figure S5B). However, in the SVZ this class of NPCs represents a fraction of ~1% of the Nes-GFP$^+$ cells, which is presumably far too small to translate into a meaningful neurogenic response (Figure S5A).

Mitochondrial respiration is the major source of cellular ROS (Jensen, 1966; Zorov et al., 2014), and mitochondrial maturation is critically linked to proliferation and progression through the developmental stages of neurogenesis (Beckervordersandforth et al., 2017). We thus asked whether the acute ROS surge seen after 1 night of running was driven by mitochondrial ROS (mitoROS) production. We tested this using MitoSOX red (Robinson et al., 2006), a mitochondria-specific version of DHE. Compared with standard-housed mice, we found no changes in distribution of Nes-GFP$^+$ cells and, more important, no discernable increase in mitoROS (two-way ANOVA: no difference for housing; Figures S5C–S5D), suggesting other sources for the ROS surge after the acute run stimulus.

Cell-Autonomous Nox2 Activity Drives Initial Responses to Physical Activity

Besides mitochondria, the other major source of cellular ROS is the Nox enzyme complex (Nox; Le Belle et al., 2011; Dickinson et al., 2011). We first analyzed Nes-GFP$^+$ cells of the different ROS classes for their transcript expression of Nox isoforms. Although we found no expression of some Nox transcripts (*Nox1*, *Nox3*, *Duox1*, or *Duox2*) coding for the plasma membrane-bound Nox2 complex, including the core components Nox2 (*Cybb*), p22phox (*Cyba*) and the cytosolic p67phox (*Ncf2*) were highest in the hiROS cells. Expression of other components of the complex (*Ncf4*, *Rac1*, *Rac2*) was maintained in cells of the hiROS and midROS classes. Interestingly, the transcript levels of

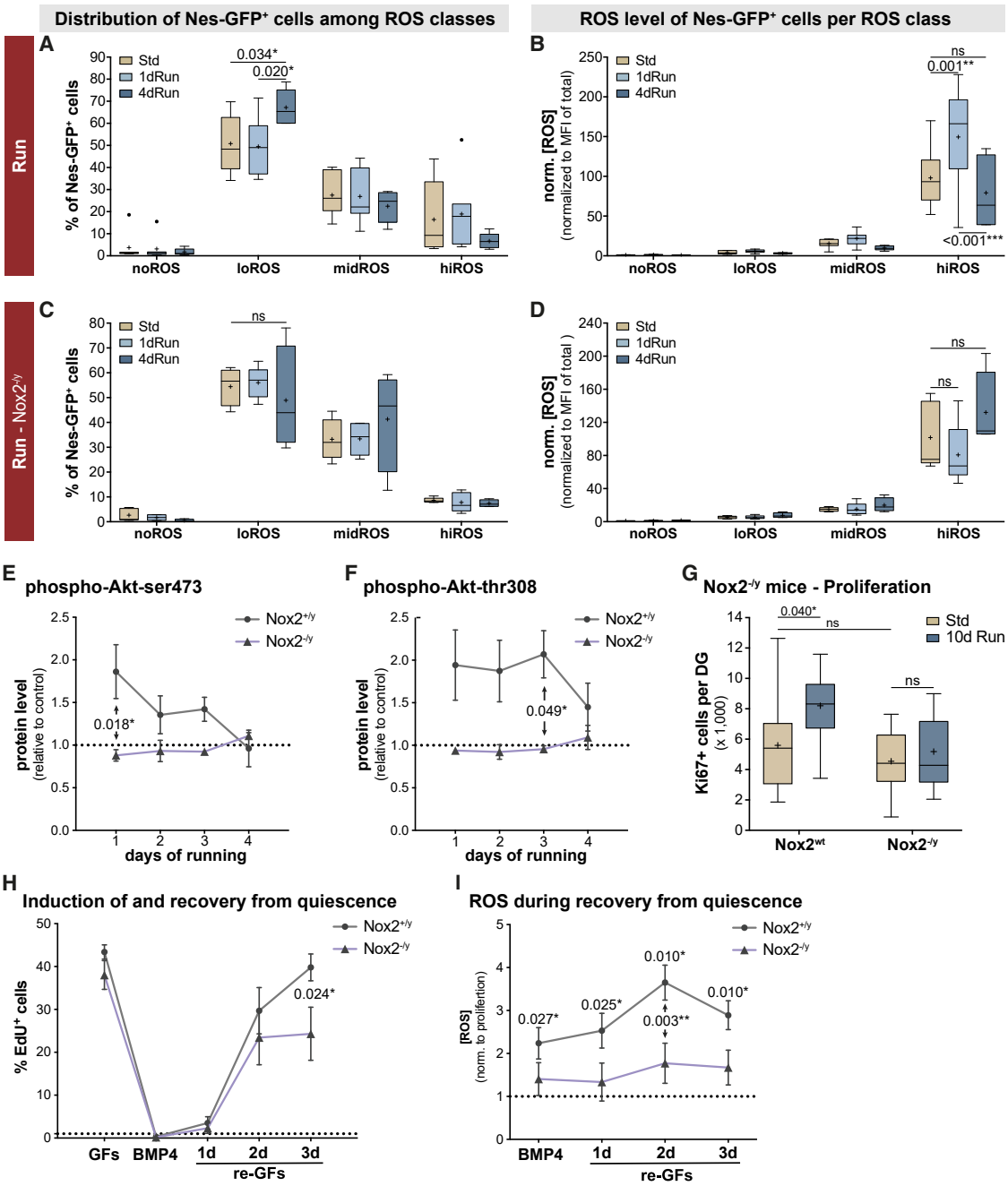

Figure 6. Nox2-Mediated ROS Fluctuations in the hi-ROS Fraction of Nes-GFP+ Cells Are Critical for Physical Activity-Mediated Precursor Activation

(A–D) Distribution of Nes-GFP$^+$ cells (A and C) and normalized ROS content (B and D) across the four ROS classes in response to physical activity in wild-type or Nox$^{-/y}$ mice (see also Figures S5E and S5F).

(E and F) Relative levels of pAkt (Ser473, E; Thr308, F) following the indicated bouts of physical activity (normalized to standard-housed mice).

(G) Number of Ki67$^+$ cells increases in the wild-type but not the Nox2 mutant animals after 10 day physical activity paradigm.

(H and I) Relative fractions of proliferating NPCs (H) and relative ROS levels (I) following BMP4 treatment and after re-plating cells with growth factors.

The horizontal line within the boxplots indicates the median, and the + sign denotes the mean. Other data represent mean ± SEM.

Cyba, *Cybb*, and *Ncf2* decreased significantly at the ROS transition from hiROS to midROS, and most transcripts of the Nox2 complex components were not detected in the loROS cells (Figures S5G and S5H). This expression pattern strongly suggests that the Nox2 complex might, on demand, produce ROS specifically in hiROS cells. We thus generated Nes-GFP::Nox2$^{-/y}$ mice and analyzed ROS profiles in this mouse model. Under baseline conditions, we saw no change in the distribution of Nes-GFP$^+$

cells among ROS classes (two-way ANOVA; genotype: p = 0.965, $F_{1,40} < 0.01$; Figure S5E) with similar ROS profiles (two-way ANOVA; genotype: p = 0.847, $F_{1,40} = 0.04$; Figure S5F) for Nox2$^{-/y}$ mutants and their wild-type (WT) littermates. Neither 1 nor 4 nights of physical activity led to a redistribution of Nox2-deficient Nes-GFP^{+} cells among the ROS classes (two-way ANOVA; housing: p = 0.997, $F_{2,44} < 0.01$; Figure 6C). Furthermore, no ROS surge was detected in the mutant Nes-GFP^{+} cells of the hiROS class after 1 or 4 nights of running (two-way ANOVA, housing: p = 0.127, $F_{2,44} = 2.17$; Figure 6D). We inferred, therefore, that Nox2 activity must drive the ROS fluctuations observed in WT mice following *de novo* physical activity.

To study downstream effects of Nox2-mediated ROS fluctuations, we investigated the established downstream target PTEN (Le Belle et al., 2011; Hervera et al., 2018). As PTEN oxidation is highly transient (Kwon et al., 2004; Schwertassek et al., 2014) and we were unable to detect significant changes in oxidized PTEN after physical activity (Figure S6A), we analyzed the relative levels of phospho-AKT (pAKT), an established target of PTEN oxidation (Covey et al., 2007; Wu et al., 2013; Silva et al., 2008) as a more stable measure of Nox2 activity (Figures 6E, 6F, and S6B). We detected an increase in the relative levels of pAkt-ser473 after 1 night of physical activity in WT animals compared with Nox2 mutants (two-way ANOVA, genotype: p = 0.010, $F_{1,24} = 7.82$; Sidak, p = 0.018; Figure 6E). Furthermore, in the Nox2 WT animals, increased levels of pAkt-thr308 were maintained for longer durations and, compared with the mutants, were significantly upregulated after 3 nights of physical activity (two-way ANOVA, genotype: $p < 0.001$, $F_{1,24} = 17.79$; Sidak, p = 0.049; Figure 6F).

To confirm that the Nox2-mediated ROS surge and the downstream effects are indeed essential for the pro-neurogenic response, we quantified proliferating Ki67^{+} cells in the DG of WT and Nox2 mutants using a longer 10-night physical activity paradigm to ensure that we captured any delayed increases in proliferation (Kronenberg et al., 2003; Overall et al., 2013). Under baseline conditions, Nox2-deficient animals had similar proliferation rates compared with WT littermates (two-way ANOVA; genotype: p = 0.004, $F_{1,46} = 9.24$, housing: p = 0.019, $F_{1,46} = 5.88$; Tukey: WT-Std versus Nox2$^{-/y}$-Std p = 0.701; Figure 6G). Although physical activity increased the number of Ki67^{+} cells in WT animals (p = 0.040), this increase was absent in the Nox2$^{-/y}$ mice (p = 0.907; Figure 6G). Furthermore, whereas in an *ex vivo* NS assay, KCl strongly stimulated the formation of NS from WT littermates, we did not see a similar effect in cells isolated from Nox2 mutant animals (two-way ANOVA, matched within genotypes; interaction: p = 0.002, $F_{1,19} = 12.97$; Sidak: Nox2$^{+/y}$ $p < 0.001$, Nox2$^{-/y}$ p = 0.686; Figure S5I). Taken together, these results show that Nox2, although not required for baseline proliferation, is essential for the pro-proliferative response to physical activity.

Ex Vivo and *In Vitro* Models Establish the Correlation between Cellular States and Cell-Autonomous Nox2 Activity

To determine the cellular specificity of Nox2 activity and the role of Nox2-dependent ROS dynamics in cell cycle entry, we generated homogeneous monolayer NPC cultures from Nox2$^{-/y}$ mice and their Nox2$^{+/y}$ littermates. In both cultures, BMP4 treatment led to entry into quiescence (Figures 6H and S6C). However, although the transition in the WT NPC cultures was marked by an increase in cellular ROS levels (2.24 ± 0.36-fold; one-sample t test with FDR correction, $p_{adj} = 0.027$; Figure 6I), only a very dampened ROS increase was observed in Nox2 mutant cultures (1.40 ± 0.38-fold, one-sample t test, $p_{adj} = 0.349$, ns; Figure 6I).

Upon re-plating BMP4-treated cells into proliferation medium, both cultures started to revert back to active cell cycle (Figures 6H and S6C). However, the reversion in WT NPCs was distinctly pro-oxidative. Two days after return to proliferation conditions, the increase in the fraction of cells re-entering cell cycle was concomitant with a significant ROS surge (3.65 ± 0.41-fold increased ROS levels; $p_{adj} = 0.010$; Figure 6I). These ROS fluctuations were absent in the mutant NPCs ($p_{adj} = 0.174$; one-sample t test; Figure 6I). By day 3, the proliferative fraction in reverted WT NPCs returned to levels observed in control conditions. The mutant NPCs, however, leveled off from day 2 (two-way ANOVA, genotype: p = 0.019, $F_{1,40} = 6.00$; Sidak for day 3: p = 0.024; Figure 6I), indicating that fewer Nox2$^{-/y}$ cells re-entered proliferation following BMP4 treatment.

These *in vitro* results further reinforce our *in vivo* findings that although Nox2 activity is not required to maintain cells in a constant baseline proliferative state, cell-autonomous Nox2-dependent ROS dynamics promote the exit from quiescence of adult hippocampal neural stem cells.

DISCUSSION

Unlike other stem cell niches in the adult (especially in the bone marrow), the NPCs in the DG are surrounded by their long-lasting progeny, the granule neurons. A dedicated neuronal machinery protects the neurons from the detrimental effects of intracellular ROS. Stem cells, however, use intrinsic ROS as intracellular messenger molecules, especially for cell cycle-related events (Chiu and Dawes, 2012). Our results demonstrate that the NPCs within the DG maintain relatively high levels of ROS compared with their terminally differentiated progeny, and we postulate that this redox disequilibrium is necessary for an active stem cell niche, allowing (1) an unambiguous, unidirectional gradient from quiescent hiROS NPCs to low or noROS neurons and (2) creation of a subset of NPCs responsive to environmental stimuli. Indeed, we show that physical activity recruits a subset of quiescent stem cells into active cell cycle (rather than acting as a survival or expansion cue) via mechanisms independent from baseline establishment of neurogenic homeostasis. This is in line with reported effects of acute voluntary exercise on quiescent Hopx-GFP^{+} NPCs (Berg et al., 2019).

Our results demonstrate that RGL cells are functionally heterogeneous. We provide evidence for at least two different non-proliferative NPC cellular states, both of which continue to express RGL and quiescence markers but are marked by distinctly different cellular ROS levels. The subset of cells with the highest cellular ROS content are transcriptionally characterized by (1) the restricted gene expression of bona fide quiescent stem cell markers, (2) the complete absence of transcripts for *Eomes* (Tbr2) and *E2f1*, and (3) significantly lower expression of proliferation markers. On the basis of these criteria, we propose that these Nes-GFP^{+} cells of the hiROS class have the lowest probability of cell cycle entry and represent the long-

term quiescent NPC pool. Through a drastic shift in intracellular ROS content, hiROS Nes-GFP$^+$ convert to a poised subset of NPCs that have only moderate cellular ROS content (midROS Nes-GFP$^+$ pool), which are still quiescent but primed for entering the cell cycle. The increased probability of exit from quiescence can be inferred from a marked reduction in transcripts for key cell cycle inhibitors and an upregulation of transcripts necessary for proliferation. We argue, therefore, that changes in ROS may precede other metabolic changes which are necessary for entry into an active growth phase, such as the shift from FAO to lipogenesis (Knobloch and Jessberger, 2017; Knobloch et al., 2017) or the shift to oxidative phosphorylation as the major energy source in the NPCs (Beckervordersandforth et al., 2017; Zheng et al., 2016). Cells seemingly preserve the moderate cellular ROS levels as they traverse through transient amplification.

We further speculate that the second reproducible ROS shift marks the transition into a NB-like identity, characterized by reduced proliferation and a more neuronal profile. We could reproduce these cytometry-based findings in adherent cell culture, indicating that the observed ROS profiles were not artifacts of dissociation and sorting. Our results suggest that hippocampal neurogenic niche is characterized by a gradient of reducing cellular ROS content that is correlated with cell cycle entry, neurogenic progression, and neuronal lineage commitment. Our annotation of cellular identities within each ROS class aligns well with the trajectories proposed by Shin et al. (2015) and the work of Linnarsson and colleagues (Hochgerner et al., 2018).

Previous work has shown that oxidation and inactivation of plasma membrane-bound PTEN acts as a potential downstream target of Nox2 (Le Belle et al., 2011; Hervera et al., 2018), and transient inactivation of PTEN triggers Akt phosphorylation, a more stable cellular readout. Akt activation influences cellular growth and proliferation (Luo et al., 2003), and we thus suggest that the observed Nox2-mediated increase in phosphorylated Akt levels results in increased cell cycle entry (Bruel-Jungerman et al., 2009) and thereby the observed redistribution of Nes-GFP$^+$ cells into the ROS classes, which was absent in Nox2-deficient mice.

The present study proposes Nox-dependent ROS fluctuation as an early cellular signaling event mediating the pro-proliferative response of the adult hippocampal neurogenic niche to environmental cues. We hope future work will show how ROS signaling links to the later processes controlling hippocampal NPC proliferation and neuronal commitment.

Limitations of Study

The present study, while identifying distinct functional states by resolving NPCs for cellular ROS content, does not extend to describing the processes which establish and regulate the changes in cellular ROS status leading to cellular state transitions. The work was also limited by the availability and the fluorescent range compatibility of genetically encoded ROS sensors, which might enable observation of longitudinal redox changes *in vivo*. Furthermore, although our work identifies Nox2-mediated ROS fluctuations as the first cell-autonomous response to physical activity, it does not highlight how physical activity at the organism scale leads to cell-autonomous activation of Nox2.

STAR★METHODS

Detailed methods are provided in the online version of this paper and include the following:

- KEY RESOURCES TABLE
- RESOURCE AVAILABILITY
  - Lead Contact
  - Materials Availability
  - Data and Code Availability
- EXPERIMENTAL MODEL AND SUBJECT DETAILS
  - Mice
- METHOD DETAILS
  - Thymidine labeling and tissue preparation
  - Fluorescence immunohistochemistry
  - DG and SVZ dissection and dissociation
  - Flow cytometry
  - Gating for ROS classes
  - Neurosphere culture
  - Generation of monolayer culture
  - Inducing quiescence through BMP4 treatment
  - ROS profiling of *in vivo* proliferating cells
  - Next Generation sequencing
  - Quality control and differential expression
  - Functional enrichment and expression profiles
  - RNA isolation and quantitative RTPCR (q-RTPCR)
  - Cycling conditions for q-RTPCRs
  - Ki67 immunohistochemistry and quantification of *in vivo* proliferation
  - Protein electrophoresis and western blot analysis
- QUANTIFICATION AND STATISTICAL ANALYSIS

SUPPLEMENTAL INFORMATION

Supplemental Information can be found online at https://doi.org/10.1016/j.stem.2020.10.019.

ACKNOWLEDGMENTS

This work was supported by the flow cytometry core facility of the Center for Regenerative Therapies Dresden (CRTD) and the DRESDEN-concept Genome Center (DDcGC) at Technische Universität Dresden. We would like to acknowledge the support of the present and past animal keepers, Nicole Rund, Anne Karasinsky, and Sandra Günther. D.G.K. is a member of the Dresden International Graduate School for Biomedicine and Bioengineering (DIGS-BB) PhD program. J.M. is supported by the German Research Foundation (DFG; Emmy Noether; MA 5831/1-1) and receives funding from the European Research Council (ERC) under the European Union's Horizon 2020 research and innovation program (grant agreement 680042). This work was funded by the VI-510 "RNA metabolism in ALS and FTD" and the AMPro consortium of the Helmholtz Association.

AUTHOR CONTRIBUTIONS

Conceptualization, V.S.A., A.E.R., and G.K.; Methodology, V.S.A., T.L.W., A.E.R., R.W.O., D.G.K., A.M.S., S.R., and A.D.; Investigation, V.S.A., T.L.W., A.E.R., S.A.Z., G.M.K., T.J.F., S.Z., and K.N.; Software and Data Curation, R.W.O.; Formal Analysis, V.S.A., A.E.R., and R.W.O.; Visualization, A.E.R. and R.W.O.; Writing – Original Draft, V.S.A., A.E.R., and G.K.; Writing – Review & Editing, T.L.W., R.W.O., S.Z., J.M., and G.K.; Supervision, A.E.R., J.M., and G.K.; Project Administration: A.E.R. and G.K.; Funding Acquisition, G.K.

DECLARATION OF INTERESTS

The authors declare no competing interests.

Received: July 17, 2020
Revised: October 14, 2020
Accepted: October 29, 2020
Published: December 3, 2020

REFERENCES

Akers, K.G., Martinez-Canabal, A., Restivo, L., Yiu, A.P., De Cristofaro, A., Hsiang, H.-L.L., Wheeler, A.L., Guskjolen, A., Niibori, Y., Shoji, H., et al. (2014). Hippocampal neurogenesis regulates forgetting during adulthood and infancy. Science *344*, 598–602.

Alexa, A., and Rahnenfuhrer, J. (2018). topGO: Enrichment Analysis for Gene Ontology (R package version 2.34.0). https://bioconductor.org/packages/release/bioc/html/topGO.html.

Andersen, J., Urbán, N., Achimastou, A., Ito, A., Simic, M., Ullom, K., Martynoga, B., Lebel, M., Göritz, C., Frisén, J., et al. (2014). A transcriptional mechanism integrating inputs from extracellular signals to activate hippocampal stem cells. Neuron *83*, 1085–1097.

Armenteros, T., Andreu, Z., Hortigüela, R., Lie, D.C., and Mira, H. (2018). BMP and WNT signalling cooperate through LEF1 in the neuronal specification of adult hippocampal neural stem and progenitor cells. Sci. Rep. *8*, 9241.

Armstrong, L., Tilgner, K., Saretzki, G., Atkinson, S.P., Stojkovic, M., Moreno, R., Przyborski, S., and Lako, M. (2010). Human induced pluripotent stem cell lines show stress defense mechanisms and mitochondrial regulation similar to those of human embryonic stem cells. Stem Cells *28*, 661–673.

Babu, H., Cheung, G., Kettenmann, H., Palmer, T.D., and Kempermann, G. (2007). Enriched monolayer precursor cell cultures from micro-dissected adult mouse dentate gyrus yield functional granule cell-like neurons. PLoS ONE *2*, e388.

Babu, H., Claasen, J.-H., Kannan, S., Rünker, A.E., Palmer, T., and Kempermann, G. (2011). A protocol for isolation and enriched monolayer cultivation of neural precursor cells from mouse dentate gyrus. Front. Neurosci. *5*, 89.

Beckervordersandforth, R., Ebert, B., Schäffner, I., Moss, J., Fiebig, C., Shin, J., Moore, D.L., Ghosh, L., Trinchero, M.F., Stockburger, C., et al. (2017). Role of mitochondrial metabolism in the control of early lineage progression and aging phenotypes in adult hippocampal neurogenesis. Neuron *93*, 560–573.e6.

Bedford, L., Walker, R., Kondo, T., van Crüchten, I., King, E.R., and Sablitzky, F. (2005). Id4 is required for the correct timing of neural differentiation. Dev. Biol. *280*, 386–395.

Berg, D.A., Su, Y., Jimenez-Cyrus, D., Patel, A., Huang, N., Morizet, D., Lee, S., Shah, R., Ringeling, F.R., Jain, R., et al. (2019). A common embryonic origin of stem cells drives developmental and adult neurogenesis. Cell *177*, 654–668.e15.

Bigarella, C.L., Liang, R., and Ghaffari, S. (2014). Stem cells and the impact of ROS signaling. Development *141*, 4206–4218.

Black, E.P., Hallstrom, T., Dressman, H.K., West, M., and Nevins, J.R. (2005). Distinctions in the specificity of E2F function revealed by gene expression signatures. Proc. Natl. Acad. Sci. U S A *102*, 15948–15953.

Boareto, M., Iber, D., and Taylor, V. (2017). Differential interactions between Notch and ID factors control neurogenesis by modulating Hes factor autoregulation. Development *144*, 3465–3474.

Bonaguidi, M.A., Wheeler, M.A., Shapiro, J.S., Stadel, R.P., Sun, G.J., Ming, G.L., and Song, H. (2011). In vivo clonal analysis reveals self-renewing and multipotent adult neural stem cell characteristics. Cell *145*, 1142–1155.

Brandt, M.D., Hübner, M., and Storch, A. (2012). Brief report: adult hippocampal precursor cells shorten S-phase and total cell cycle length during neuronal differentiation. Stem Cells *30*, 2843–2847.

Brown, J., Cooper-Kuhn, C.M., Kempermann, G., Van Praag, H., Winkler, J., Gage, F.H., and Kuhn, H.G. (2003). Enriched environment and physical activity stimulate hippocampal but not olfactory bulb neurogenesis. Eur. J. Neurosci. *17*, 2042–2046.

Bruel-Jungerman, E., Veyrac, A., Dufour, F., Horwood, J., Laroche, S., and Davis, S. (2009). Inhibition of PI3K-Akt signaling blocks exercise-mediated enhancement of adult neurogenesis and synaptic plasticity in the dentate gyrus. PLoS ONE *4*, e7901.

Buck, S.B., Bradford, J., Gee, K.R., Agnew, B.J., Clarke, S.T., and Salic, A. (2008). Detection of S-phase cell cycle progression using 5-ethynyl-2′-deoxyuridine incorporation with click chemistry, an alternative to using 5-bromo-2′-deoxyuridine antibodies. Biotechniques *44*, 927–929.

Chiu, J., and Dawes, I.W. (2012). Redox control of cell proliferation. Trends Cell Biol. *22*, 592–601.

Codega, P., Silva-Vargas, V., Paul, A., Maldonado-Soto, A.R., Deleo, A.M., Pastrana, E., and Doetsch, F. (2014). Prospective identification and purification of quiescent adult neural stem cells from their in vivo niche. Neuron *82*, 545–559.

Coles-Takabe, B.L.K., Brain, I., Purpura, K.A., Karpowicz, P., Zandstra, P.W., Morshead, C.M., and van der Kooy, D. (2008). Don't look: growing clonal versus nonclonal neural stem cell colonies. Stem Cells *26*, 2938–2944.

Cooper-Kuhn, C.M., Vroemen, M., Brown, J., Ye, H., Thompson, M.A., Winkler, J., and Kuhn, H.G. (2002). Impaired adult neurogenesis in mice lacking the transcription factor E2F1. Mol. Cell. Neurosci. *21*, 312–323.

Covey, T.M., Edes, K., and Fitzpatrick, F.A. (2007). Akt activation by arachidonic acid metabolism occurs via oxidation and inactivation of PTEN tumor suppressor. Oncogene *26*, 5784–5792.

Dickinson, B.C., Peltier, J., Stone, D., Schaffer, D.V., and Chang, C.J. (2011). Nox2 redox signaling maintains essential cell populations in the brain. Nat. Chem. Biol. *7*, 106–112.

Dikalov, S.I., and Harrison, D.G. (2014). Methods for detection of mitochondrial and cellular reactive oxygen species. Antioxid. Redox Signal. *20*, 372–382.

Dobin, A., Davis, C.A., Schlesinger, F., Drenkow, J., Zaleski, C., Jha, S., Batut, P., Chaisson, M., and Gingeras, T.R. (2013). STAR: ultrafast universal RNA-seq aligner. Bioinformatics *29*, 15–21.

Doetsch, F. (2003). The glial identity of neural stem cells. Nat. Neurosci. *6*, 1127–1134.

Fischer, T.J., Walker, T.L., Overall, R.W., Brandt, M.D., and Kempermann, G. (2014). Acute effects of wheel running on adult hippocampal precursor cells in mice are not caused by changes in cell cycle length or S phase length. Front. Neurosci. *8*, 314.

Gao, Z., Ure, K., Ding, P., Nashaat, M., Yuan, L., Ma, J., Hammer, R.E., and Hsieh, J. (2011). The master negative regulator REST/NRSF controls adult neurogenesis by restraining the neurogenic program in quiescent stem cells. J. Neurosci. *31*, 9772–9786.

Garthe, A., Behr, J., and Kempermann, G. (2009). Adult-generated hippocampal neurons allow the flexible use of spatially precise learning strategies. PLoS ONE *4*, e5464.

Gebara, E., Bonaguidi, M.A., Beckervordersandforth, R., Sultan, S., Udry, F., Gijs, P.-J., Lie, D.C., Ming, G.-L., Song, H., and Toni, N. (2016). Heterogeneity of radial glia-like cells in the adult hippocampus. Stem Cells *34*, 997–1010.

Gong, S., Zheng, C., Doughty, M.L., Losos, K., Didkovsky, N., Schambra, U.B., Nowak, N.J., Joyner, A., Leblanc, G., Hatten, M.E., and Heintz, N. (2003). A gene expression atlas of the central nervous system based on bacterial artificial chromosomes. Nature *425*, 917–925.

Gurusamy, N., Mukherjee, S., Lekli, I., Bearzi, C., Bardelli, S., and Das, D.K. (2009). Inhibition of ref-1 stimulates the production of reactive oxygen species and induces differentiation in adult cardiac stem cells. Antioxid. Redox Signal. *11*, 589–600.

Hagihara, H., Toyama, K., Yamasaki, N., and Miyakawa, T. (2009). Dissection of hippocampal dentate gyrus from adult mouse. J. Vis. Exp. (33), 1543.

Hatakeyama, J., Bessho, Y., Katoh, K., Ookawara, S., Fujioka, M., Guillemot, F., and Kageyama, R. (2004). Hes genes regulate size, shape and histogenesis of the nervous system by control of the timing of neural stem cell differentiation. Development *131*, 5539–5550.

Hervera, A., De Virgiliis, F., Palmisano, I., Zhou, L., Tantardini, E., Kong, G., Hutson, T., Danzi, M.C., Perry, R.B.-T., Santos, C.X.C., et al. (2018). Reactive oxygen species regulate axonal regeneration through the release of exosomal NADPH oxidase 2 complexes into injured axons. Nat. Cell Biol. *20*, 307–319.

Hill, R., and Wu, H. (2009). PTEN, stem cells, and cancer stem cells. J. Biol. Chem. *284*, 11755–11759.

Hochgerner, H., Zeisel, A., Lönnerberg, P., and Linnarsson, S. (2018). Conserved properties of dentate gyrus neurogenesis across postnatal development revealed by single-cell RNA sequencing. Nat. Neurosci. *21*, 290–299.

Hodge, R.D., Nelson, B.R., Kahoud, R.J., Yang, R., Mussar, K.E., Reiner, S.L., and Hevner, R.F. (2012). Tbr2 is essential for hippocampal lineage progression from neural stem cells to intermediate progenitors and neurons. J. Neurosci. *32*, 6275–6287.

Holmström, K.M., and Finkel, T. (2014). Cellular mechanisms and physiological consequences of redox-dependent signalling. Nat. Rev. Mol. Cell Biol. *15*, 411–421.

Jang, M.-H., Bonaguidi, M.A., Kitabatake, Y., Sun, J., Song, J., Kang, E., Jun, H., Zhong, C., Su, Y., Guo, J.U., et al. (2013). Secreted frizzled-related protein 3 regulates activity-dependent adult hippocampal neurogenesis. Cell Stem Cell *12*, 215–223.

Jensen, P.K. (1966). Antimycin-insensitive oxidation of succinate and reduced nicotinamide-adenine dinucleotide in electron-transport particles II. Steroid effects. Biochim. Biophys. Acta *122*, 167–174.

Jhaveri, D.J., Mackay, E.W., Hamlin, A.S., Marathe, S.V., Nandam, L.S., Vaidya, V.A., and Bartlett, P.F. (2010). Norepinephrine directly activates adult hippocampal precursors via beta3-adrenergic receptors. J. Neurosci. *30*, 2795–2806.

Kempermann, G., Kuhn, H.G., and Gage, F.H. (1997). More hippocampal neurons in adult mice living in an enriched environment. Nature *386*, 493–495.

Kempermann, G., Jessberger, S., Steiner, B., and Kronenberg, G. (2004). Milestones of neuronal development in the adult hippocampus. Trends Neurosci. *27*, 447–452.

Kim, E.J., Ables, J.L., Dickel, L.K., Eisch, A.J., and Johnson, J.E. (2011). Ascl1 (Mash1) defines cells with long-term neurogenic potential in subgranular and subventricular zones in adult mouse brain. PLoS ONE *6*, e18472.

Klempin, F., Beis, D., Mosienko, V., Kempermann, G., Bader, M., and Alenina, N. (2013). Serotonin is required for exercise-induced adult hippocampal neurogenesis. J. Neurosci. *33*, 8270–8275.

Knobloch, M., and Jessberger, S. (2017). Metabolism and neurogenesis. Curr. Opin. Neurobiol. *42*, 45–52.

Knobloch, M., Braun, S.M.G., Zurkirchen, L., von Schoultz, C., Zamboni, N., Araúzo-Bravo, M.J., Kovacs, W.J., Karalay, O., Suter, U., Machado, R.A.C., et al. (2013). Metabolic control of adult neural stem cell activity by Fasn-dependent lipogenesis. Nature *493*, 226–230.

Knobloch, M., von Schoultz, C., Zurkirchen, L., Braun, S.M.G., Vidmar, M., and Jessberger, S. (2014). SPOT14-positive neural stem/progenitor cells in the hippocampus respond dynamically to neurogenic regulators. Stem Cell Reports *3*, 735–742.

Knobloch, M., Pilz, G.-A., Ghesquière, B., Kovacs, W.J., Wegleiter, T., Moore, D.L., Hruzova, M., Zamboni, N., Carmeliet, P., and Jessberger, S. (2017). A Fatty Acid Oxidation-Dependent Metabolic Shift Regulates Adult Neural Stem Cell Activity. Cell Rep. *20*, 2144–2155.

Kronenberg, G., Reuter, K., Steiner, B., Brandt, M.D., Jessberger, S., Yamaguchi, M., and Kempermann, G. (2003). Subpopulations of proliferating cells of the adult hippocampus respond differently to physiologic neurogenic stimuli. J. Comp. Neurol. *467*, 455–463.

Kwon, J., Lee, S.-R., Yang, K.-S., Ahn, Y., Kim, Y.J., Stadtman, E.R., and Rhee, S.G. (2004). Reversible oxidation and inactivation of the tumor suppressor PTEN in cells stimulated with peptide growth factors. Proc. Natl. Acad. Sci. U S A *101*, 16419–16424.

Le Belle, J.E., Orozco, N.M., Paucar, A.A., Saxe, J.P., Mottahedeh, J., Pyle, A.D., Wu, H., and Kornblum, H.I. (2011). Proliferative neural stem cells have high endogenous ROS levels that regulate self-renewal and neurogenesis in a PI3K/Akt-dependant manner. Cell Stem Cell *8*, 59–71.

Liao, Y., Smyth, G.K., and Shi, W. (2013). The Subread aligner: fast, accurate and scalable read mapping by seed-and-vote. Nucleic Acids Res. *41*, e108.

Lugert, S., Basak, O., Knuckles, P., Haussler, U., Fabel, K., Götz, M., Haas, C.A., Kempermann, G., Taylor, V., and Giachino, C. (2010). Quiescent and active hippocampal neural stem cells with distinct morphologies respond selectively to physiological and pathological stimuli and aging. Cell Stem Cell *6*, 445–456.

Luo, J., Manning, B.D., and Cantley, L.C. (2003). Targeting the PI3K-Akt pathway in human cancer: rationale and promise. Cancer Cell *4*, 257–262.

Martynoga, B., Mateo, J.L., Zhou, B., Andersen, J., Achimastou, A., Urbán, N., van den Berg, D., Georgopoulou, D., Hadjur, S., Wittbrodt, J., et al. (2013). Epigenomic enhancer annotation reveals a key role for NFIX in neural stem cell quiescence. Genes Dev. *27*, 1769–1786.

Nolte, C., Matyash, M., Pivneva, T., Schipke, C.G., Ohlemeyer, C., Hanisch, U.K., Kirchhoff, F., and Kettenmann, H. (2001). GFAP promoter-controlled EGFP-expressing transgenic mice: a tool to visualize astrocytes and astrogliosis in living brain tissue. Glia *33*, 72–86.

Overall, R.W., Walker, T.L., Leiter, O., Lenke, S., Ruhwald, S., and Kempermann, G. (2013). Delayed and transient increase of adult hippocampal neurogenesis by physical exercise in DBA/2 mice. PLoS ONE *8*, e83797.

Overall, R.W., Walker, T.L., Fischer, T.J., Brandt, M.D., and Kempermann, G. (2016). Different mechanisms must be considered to explain the increase in hippocampal neural precursor cell proliferation by physical activity. Front. Neurosci. *10*, 362.

Pechnick, R.N., Zonis, S., Wawrowsky, K., Pourmorady, J., and Chesnokova, V. (2008). p21Cip1 restricts neuronal proliferation in the subgranular zone of the dentate gyrus of the hippocampus. Proc. Natl. Acad. Sci. U S A *105*, 1358–1363.

Phaniendra, A., Jestadi, D.B., and Periyasamy, L. (2015). Free radicals: properties, sources, targets, and their implication in various diseases. Indian J. Clin. Biochem. *30*, 11–26.

Pollock, J.D., Williams, D.A., Gifford, M.A.C., Li, L.L., Du, X., Fisherman, J., Orkin, S.H., Doerschuk, C.M., and Dinauer, M.C. (1995). Mouse model of X-linked chronic granulomatous disease, an inherited defect in phagocyte superoxide production. Nat. Genet. *9*, 202–209.

Reynolds, B.A., and Weiss, S. (1992). Generation of neurons and astrocytes from isolated cells of the adult mammalian central nervous system. Science *255*, 1707–1710.

Rietze, R.L., and Reynolds, B.A. (2006). Neural stem cell isolation and characterization. Methods Enzymol. *419*, 3–23.

Robinson, K.M., Janes, M.S., Pehar, M., Monette, J.S., Ross, M.F., Hagen, T.M., Murphy, M.P., and Beckman, J.S. (2006). Selective fluorescent imaging of superoxide in vivo using ethidium-based probes. Proc. Natl. Acad. Sci. U S A *103*, 15038–15043.

Robinson, M.D., McCarthy, D.J., and Smyth, G.K. (2010). edgeR: a Bioconductor package for differential expression analysis of digital gene expression data. Bioinformatics *26*, 139–140.

Sahay, A., Scobie, K.N., Hill, A.S., O'Carroll, C.M., Kheirbek, M.A., Burghardt, N.S., Fenton, A.A., Dranovsky, A., and Hen, R. (2011). Increasing adult hippocampal neurogenesis is sufficient to improve pattern separation. Nature *472*, 466–470.

Schwertassek, U., Haque, A., Krishnan, N., Greiner, R., Weingarten, L., Dick, T.P., and Tonks, N.K. (2014). Reactivation of oxidized PTP1B and PTEN by thioredoxin 1. FEBS J. *281*, 3545–3558.

Sellgren, C.M., Sheridan, S.D., Gracias, J., Xuan, D., Fu, T., and Perlis, R.H. (2017). Patient-specific models of microglia-mediated engulfment of synapses and neural progenitors. Mol. Psychiatry *22*, 170–177.

Semerci, F., Choi, W.T.-S., Bajic, A., Thakkar, A., Encinas, J.M., Depreux, F., Segil, N., Groves, A.K., and Maletic-Savatic, M. (2017). Lunatic fringe-mediated Notch signaling regulates adult hippocampal neural stem cell maintenance. eLife *6*, e24660.

Shibui, S., Hoshino, T., Vanderlaan, M., and Gray, J.W. (1989). Double labeling with iodo- and bromodeoxyuridine for cell kinetics studies. J. Histochem. Cytochem. *37*, 1007–1011.

Shin, J., Berg, D.A., Zhu, Y., Shin, J.Y., Song, J., Bonaguidi, M.A., Enikolopov, G., Nauen, D.W., Christian, K.M., Ming, G.L., and Song, H. (2015). Single-cell RNA-seq with Waterfall reveals molecular cascades underlying adult neurogenesis. Cell Stem Cell *17*, 360–372.

Silva, A., Yunes, J.A., Cardoso, B.A., Martins, L.R., Jotta, P.Y., Abecasis, M., Nowill, A.E., Leslie, N.R., Cardoso, A.A., and Barata, J.T. (2008). PTEN posttranslational inactivation and hyperactivation of the PI3K/Akt pathway sustain primary T cell leukemia viability. J. Clin. Invest. *118*, 3762–3774.

Smith, J., Ladi, E., Mayer-Proschel, M., and Noble, M. (2000). Redox state is a central modulator of the balance between self-renewal and differentiation in a dividing glial precursor cell. Proc. Natl. Acad. Sci. U S A *97*, 10032–10037.

van Praag, H., Kempermann, G., and Gage, F.H. (1999). Running increases cell proliferation and neurogenesis in the adult mouse dentate gyrus. Nat. Neurosci. *2*, 266–270.

Walker, T.L., and Kempermann, G. (2014). One mouse, two cultures: isolation and culture of adult neural stem cells from the two neurogenic zones of individual mice. J. Vis. Exp. (84), e51225.

Walker, T.L., Yasuda, T., Adams, D.J., and Bartlett, P.F. (2007). The doublecortin-expressing population in the developing and adult brain contains multipotential precursors in addition to neuronal-lineage cells. J. Neurosci. *27*, 3734–3742.

Walker, T.L., White, A., Black, D.M., Wallace, R.H., Sah, P., and Bartlett, P.F. (2008). Latent stem and progenitor cells in the hippocampus are activated by neural excitation. J. Neurosci. *28*, 5240–5247.

Walker, T.L., Overall, R.W., Vogler, S., Sykes, A.M., Ruhwald, S., Lasse, D., Ichwan, M., Fabel, K., and Kempermann, G. (2016). Lysophosphatidic acid receptor is a functional marker of adult hippocampal precursor cells. Stem Cell Reports *6*, 552–565.

Wu, K.L., Wu, C.A., Wu, C.W., Chan, S.H., Chang, A.Y., and Chan, J.Y. (2013). Redox-sensitive oxidation and phosphorylation of PTEN contribute to enhanced activation of PI3K/Akt signaling in rostral ventrolateral medulla and neurogenic hypertension in spontaneously hypertensive rats. Antioxid. Redox Signal. *18*, 36–50.

Yamaguchi, M., Saito, H., Suzuki, M., and Mori, K. (2000). Visualization of neurogenesis in the central nervous system using nestin promoter-GFP transgenic mice. Neuroreport *11*, 1991–1996.

Ye, Z.-W., Zhang, J., Townsend, D.M., and Tew, K.D. (2015). Oxidative stress, redox regulation and diseases of cellular differentiation. Biochim. Biophys. Acta *1850*, 1607–1621.

Zeng, C., Pan, F., Jones, L.A., Lim, M.M., Griffin, E.A., Sheline, Y.I., Mintun, M.A., Holtzman, D.M., and Mach, R.H. (2010). Evaluation of 5-ethynyl-2′-deoxyuridine staining as a sensitive and reliable method for studying cell proliferation in the adult nervous system. Brain Res. *1319*, 21–32.

Zheng, X., Boyer, L., Jin, M., Mertens, J., Kim, Y., Ma, L., Ma, L., Hamm, M., Gage, F.H., and Hunter, T. (2016). Metabolic reprogramming during neuronal differentiation from aerobic glycolysis to neuronal oxidative phosphorylation. eLife *5*, e13374.

Zhou, G., Meng, S., Li, Y., Ghebre, Y.T., and Cooke, J.P. (2016). Optimal ROS signaling is critical for nuclear reprogramming. Cell Rep. *15*, 919–925.

Zielonka, J., Vasquez-Vivar, J., and Kalyanaraman, B. (2008). Detection of 2-hydroxyethidium in cellular systems: a unique marker product of superoxide and hydroethidine. Nat. Protoc. *3*, 8–21.

Zorov, D.B., Juhaszova, M., and Sollott, S.J. (2014). Mitochondrial reactive oxygen species (ROS) and ROS-induced ROS release. Physiol. Rev. *94*, 909–950.

STAR★METHODS

KEY RESOURCES TABLE

REAGENT or RESOURCE	SOURCE	IDENTIFIER
Antibodies		
Rat monoclonal CD11b, FITC	Thermo Fisher Scientific	RRID:AB_11042156
Mouse monoclonal anti-IdU	BD Bioscience	RRID:AB_400326
Goat polyclonal anti-doublecortin (Dcx)	Santa Cruz	RRID:AB_2088494
Rat monoclonal anti-BrdU (CldU/BrdU)	Bio-Rad	RRID:AB_609568
Rabbit polyclonal anti-Ki67	Novocastra	RRID:AB_442102
Goat polyclonal anti-Sox2	Santa Cruz	RRID:AB_2286684
Rabbit polyclonal anti-Tbr2	Abcam	RRID:AB_778267
Mouse monoclonal anti β-actin	Cell Signaling Technology	RRID:AB_2242334
Rabbit monoclonal Akt (Pan)	Cell Signaling Technology	RRID:AB_915783
Rabbit monoclonal Phospho-Akt (ser473)	Cell Signaling Technology	RRID:AB_2315049
Rabbit monoclonal Phospho-Akt (Thr308)	Cell Signaling Technology	RRID:AB_2629447
Mouse monoclonal anti-PTEN	Santa Cruz	RRID:AB_628187
Rabbit monoclonal anti-PTEN	Abcam	RRID:AB_777535
Chemicals, Peptides, and Recombinant Proteins		
Accutase	Sigma-Aldrich	A6964
B27 supplement	Thermo Fisher Scientific	17504044
Bone morphogenic protein 4 (recombinant human BMP4)	R & D systems	314-BP-050
5-Bromo-2′-deoxyuridine (BrdU)	Sigma-Aldrich	B5002
CellROX Deep Red reagent	Thermo Fisher Scientific	C10422
5-Chloro-2′deoxyuridine (CldU)	Sigma-Aldrich	C6891
diaminobenzidine (DAB)	Sigma-Aldrich	D5905
Dihydroethidium	Thermo Fisher Scientific	D1168
EdU- Click-iT EdU Alexa Fluor 647 Flow Cytometry Assay Kit	Thermo Fisher Scientific	C10424
EDTA-free Protease inhibitor cocktail	Sigma-Aldrich	11 873 580 001
Epidermal growth factor	Peprotech	AF-100-15
Basic fibroblast growth factor	Peprotech	AF-100-18B
GlutaMAX supplement	Thermo Fisher Scientific	35050061
Heparin	MP Biomedicals	0210193125
5-Iodo-2′-deoxyuridine (IdU)	Sigma-Aldrich	I7125
Laminin	Sigma-Aldrich (Roche)	11 243 217 001
L-(-)-Noradrenaline(+)-bitartrate salt monohydrate	Merck	A9512
Neurobasal medium	Thermo Fisher Scientific	21103049
MitoSOX	Thermo Fisher Scientific	M36008
Neo-Clear	Merck	109843
Neo-Mount	Merck	109016
eBioscience Fixable Viability Dye eFluor780	Thermo Fisher Scientific	65-0865-14
PhosSTOP phosphatase inhibitor	Sigma-Aldrich	04 906 845 001
Propidium Iodide	Thermo Fisher Scientific	P3566
Poly-D-lysine (PDL)	Sigma-Aldrich	P7280
Potassium Chloride	Sigma-Aldrich	P9333
RNaseOUT Recombinant Ribonuclease Inhibitor	Thermo Fisher Scientific	10777019
SuperScriptII Reverse Transcriptase	Thermo Fisher Scientific	18064022

(*Continued on next page*)

Continued

REAGENT or RESOURCE	SOURCE	IDENTIFIER
Critical Commercial Assays		
Advantage 2 Polymerase Mix	Takara	639201
NEBNext Ultra DNA Library Prep Kit	Miltenyi Biotec	E7645
Neural Tissue Dissociation Kit (P)	New England Biolabs	130-092-628
RNeasy Micro Kit	QIAGEN	74004
VECTASTAIN ABC-HRP Kit	Vector Laboratories	PK-4000
QuantiFast SYBR Green PCR Kit	QIAGEN	204054
SMARTer Ultra Low Input RNA - HV Kit	Takara	CLT634823
Deposited Data		
Raw Sequence data	This paper	GEO: GSE124095
Experimental Models: Organisms/Strains		
Nox2$^{-/-}$ (B6.129S-Cybb^{tm1Din}/J)	The Jackson Laboratory	RRID:IMSR_JAX:002365
C57BL/6JRj	Janvier	
Tg(Nes-EGFP)1Yamm	Yamaguchi et al., 2000	RRID:IMSR_RBRC06355
Tg(GFAP-EGFP)1Hket	Nolte et al., 2001	MGI:6188855 Frank Kirchhoff (University of Saarland, Germany)
Tg(Dcx-EGFP)BJ224Gsat/Mmmh	Gensat	RRID:MMRRC_000244-MU
NPC monolayer culture; C57BL/6JRj	Janvier	N/A
Oligonucleotides		
Actb_ q_fw	ACCCGCGAGCACAGCTTC	Product_ size: 112 bp Annealing temperature: 58-60°C
Actb_ q_rev	ACATGCCGGAGCCGTTGTC	
Ascl1_ q_fw	GGAACAAGAGCTGCTGGACT	Product_ size: 119 bp Annealing temperature: 59°C
Ascl1_ q_rev	TCGTTGGCGAGAAACACTAA	
Calb2_ q_fw	TGGAAATCTGGAAGCACTTTGA	Product_ size: 107 bp Annealing temperature: 59°C
Calb2_ q_rev	CATGCCAGAACCCTTCCTTG	
Rbfox3_ q_fw	CGGCATGACCCTCTACACAC	Product_ size: 126 bp Annealing temperature: 59°C
Rbfox3_ q_rev	TGCTGGTTGTCTGTCTGTGC	
Software and Algorithms		
Prism	GraphPad	V8
FlowJo	FLOWJO, LLC	V10
Diva	BD Biosciences	V8.01
Imagestudio	Li-Cor	5.x
R		v3.5.1

RESOURCE AVAILABILITY

Lead Contact

Further information and requests for resources and reagents should be directed to and will be fulfilled by the Lead Contact, Professor Gerd Kempermann (gerd.kempermann@dzne.de).

Materials Availability

This study did not generate new unique reagents.

Data and Code Availability

Raw RNA sequencing data for both the DG/SVZ and ROS experiments are available from GEO (http://www.ncbi.nlm.nih.gov/geo) under the SuperSeries accession GEO: GSE124095. Processed data and code to reproduce the sequencing analyses can be found at https://github.com/rupertoverall/ROS.

EXPERIMENTAL MODEL AND SUBJECT DETAILS

Mice

Mice were maintained on a 12-/12-h light/dark cycle with access to standard mouse chow (Sniff) and water *ad libitum*. Animals were aged between 6-8 weeks old at the time of the experiment, unless otherwise stated. C57BL/6JRj female mice were purchased from Janvier Labs. Nox2 knockout mice (B6.129S-Cybb^{tm1Din}/J; Pollock et al., 1995) were initially purchased from The Jackson Laboratory and maintained as a heterozygous breeding colonies, Nestin-GFP mice (Yamaguchi et al., 2000), were obtained from Yamaguchi and colleagues and maintained as a homozygous colony, Dcx-GFP mice (Stock Tg(Dcx-EGFP) BJ224Gsat/Mmmh) were purchased from Mutant Mouse Resource and Research center and maintained as a homozygous colony (Gong et al., 2003). Gfap-GFP mice were acquired from the lab of Frank Kirchhoff (University of Saarland) and maintained as a homozygous colony (Nolte et al., 2001). Mice were housed in groups of at least two mice in standard polycarbonate cages (Type III, Techniplast, Germany), except for the animals with running wheels, which were singly-housed. All experiments were conducted in accordance with the applicable European regulations and approved by the responsible authority (Landesdirektion Sachsen). Detailed information on the genotype of the animals used for each experiment; the number of animals per sample and sample size is given in Table S5.

METHOD DETAILS

Thymidine labeling and tissue preparation

To label proliferating cells, animals were injected intraperitoneally with BrdU (50 mg/kg) or CldU (42.5 mg/kg) and IdU (57.5 mg/kg). See individual experimental set-up paradigms for the timing of the labeling (Figures S1A and 1B). Mice were transcardially perfused with NaCl (0.9% w/v) followed by 4% paraformaldehyde (PFA, experiment shown in Figure S1A). Alternatively, brains were removed after NaCl perfusion (experiment in Figure 1B). All brains were post-fixed in 4% PFA at 4°C overnight. The next day, brains were transferred to a 30% sucrose solution for 2–3 days. Coronal sections with a thickness of 40 μm were cut using a sliding microtome (Leica SM2010) cooled with dry ice. Sections were collected and stored as floating sections in cryoprotection solution (CPS; 25% ethylene glycol, 25% glycerol in 0.1 M phosphate buffer pH 7.4) at −20°C. Every sixth section of each brain was pooled in one series for immunohistochemistry.

Fluorescence immunohistochemistry

Two combinations of antibodies were used to phenotype the proliferating cells (Sox2/Tbr2/IdU/CldU, or Tbr2/Dcx/IdU/CldU). Sections were first washed with PBS and treated with 0.9% NaCl, before DNA denaturation was performed in 2 N HCl for 30 min at 37°C. The sections were then thoroughly washed with PBS and blocked for 1 h in PBS supplemented with 10% donkey serum (Jackson ImmunoResearch Laboratories Inc) and 0.1% Triton X-100. Primary antibodies (Sox2, Tbr2, Dcx, rat anti-BrdU, or mouse anti-BrdU) were diluted in PBS supplemented with 3% donkey serum and 0.1% Triton X-100. Incubation was performed overnight at 4°C. After several rinses in PBS, the sections were incubated with secondary antibodies diluted in PBS supplemented with 3% donkey serum and 0.1% Triton X-100 at room temperature for 4 h. They were then washed in PBS, after which 4 ,6-diamidino-2-phenylindole (DAPI, 1:2000) staining was performed for 10 min. After a final wash with PBS, the sections were mounted on glass slides and coverslipped with Aqua-Poly/Mount (Polysciences Europe GmbH). CldU$^+$ and IdU$^+$ cells in every sixth section (240 μm apart) were counted along the complete ventral dorsal extent of the DG at 40x magnification using a Zeiss Apotome microscope. Results were multiplied by 6 in order to obtain the total number of positive cells within the DG region of each brain (related to Figure 1C). Using a Spinning Disc Zeiss Axio Observer.Z1 microscope, at least 100 CldU$^+$ or IdU$^+$ cells per DG from 3 to 4 central sections of a 1:6 series (240 μm apart) were phenotyped for double-labeling (Figure 1D) and the co-expression of Sox2 and Tbr2, or Tbr2 and Dcx (Figures 1E, 1F, S1D, and S1E).

DG and SVZ dissection and dissociation

Mice were killed, their brains immediately removed, and the dentate gyrus (DG) and SVZ microdissected (Hagihara et al., 2009; Walker and Kempermann, 2014). The tissue was enzymatically digested using the Neural Tissue Dissociation Kit (Miltenyi) according to the manufacturer's instructions. Following a final wash in Hank's balanced salt solution (HBSS; GE Healthcare) the pellet was resuspended in 1 mL of growth medium or HBSS and filtered through a 40 μm cell sieve (Falcon; BD Biosciences) for subsequent procedures.

For cellular ROS measurements, either CellROX DeepRed Reagent (5 μM, Thermo Fisher Scientific, for the neurosphere assays) or dihydroethidium (DHE; 5 μM, Thermo Fisher Scientific, for all other ROS analyses) was added to resuspended cells, along with a live/dead vitality dye (vitality dye eFluor^{TM} 780 in conjugation with DHE and Mitosox, PI in conjugation with CellROX DeepRed) and incubated for 30 min at 37°C. For mitochondrial ROS measurements MitoSOX Red Mitochondrial Superoxide indicator (5 μM, Thermo Fisher Scientific) was added and incubated for 15 min. Following incubation, the cells were centrifuged to remove excess dye, resuspended in PBS and immediately subjected to flow cytometry. During the whole procedure (in all the experiments conducted), cells were never subject to repeated staining with any dye/marker.

Flow cytometry

Dissociated SVZ or DG cells were analyzed using a FACS Aria III cell sorter (BD Biosciences) and an 85 μm nozzle. Cells were first gated based on the forward and side scatter (FSC and SSC) properties to identify the main cell population (Figure S2A). Dead cells were excluded using a live/dead dye (Figure S2B) and doublets were excluded based on the height and width of the FSC and SSC signals of events (Figures S2C and S2D). Where applicable, live single reporter-GFP-positive cells where gated (Nes-GFP: Figure S2E; Dcx-GFP: Figure 5B). Live single and/or reporter GFP-positive cells were then gated based on their ROS content (see below) for analysis or sorting. Cell populations were sorted into either medium (for neurosphere experiments), RLT buffer (for RNA isolation) or PBS (for western blot analyses).

Gating for ROS classes

The cells of the DG and SVZ yielded very stereotypical ROS profiles, which were manually clustered, based on the density of clustering cells, into 4 non-overlapping classes using DIVA (BD Biosciences) for sorting the populations or during analysis using FlowJo (V10). The gates obtained from live single DG cells (standard housing, Figure 3A) were used as the "master gates," which were applied to runner DG or SVZ cells without (SVZ: Figure 3E) or with (Nes-GFP: Figures 3J and 3K) prior gating for reporter-GFP positive cells.

Neurosphere culture

For neurosphere culture, cells were resuspended in neurosphere growth medium consisting of Neurobasal medium (GIBCO, Life Technologies), supplemented with 2% B27 (Invitrogen), 1 × GlutaMAX (Life Technologies) and 50 units/ml penicillin/streptomycin (Life Technologies). The following growth factors were also included: 20 ng/ml EGF, 20 ng/ml FGF-2 and 20 ng/ml Heparin. Cells were seeded into 96-well plates at the clonal density of approximately 5 cells/μl for SVZ and 7.5 cells/μl for DG-derived cells. This density, which has previously been described to result in the formation of clonally-derived neurospheres (Coles-Takabe et al., 2008), resulted in the formation of an average of less than one neurosphere per well in our experiments. Cells were incubated at 37°C with 5% CO2 and the resulting neurospheres counted using an inverted light microscope after either 7 days for SVZ cultures or 14 days for DG cultures. We used 15 mM KCl or L-(−)-noradrenaline (+)-bitartrate salt monohydrate (norepinephrine; 10 μM) as a stimulant to trigger latent cells to form neurospheres *in vitro*.

Generation of monolayer culture

Animals of specific genotypes were sacrificed and DG cells were isolated as described above. The isolated cells were plated on surfaces coated with poly-D-lysine (overnight coating with 50 μM dissolved in water) and laminin (overnight coating with 50 μM dissolved in PBS/DMEM incomplete medium). The monolayer cultures were maintained in the presence of growth factors: 20 ng/ml EGF, 20 ng/ml FGF-2 and incubated at 37°C with 5% CO_2 and 21% O_2. For passaging, confluent cultures were washed with PBS, the contacts broken by treatment with accutase, counted and re-plated at a density which leads to 80%–90% surface occupancy in 3-4 days. To establish homogeneous cell lines, NPCs were cultured for 5 passages and immunoassayed (IF) for the expression of Nestin and Sox2. These procedures are described in detailed in (Babu et al., 2007, 2011). Specific experiments, detailed below, were conducted on NPC after passage number 5.

Inducing quiescence through BMP4 treatment

Cells were plated at different confluencies to achieve 60%–70% at different days in either T25 or 6-well plates. Three different durations of 20 ng/ml BMP4 treatment were employed: 1 day of BMP4 treatment which included 3 days of proliferation to yield 60%–70% confluency and 1 day of EGF withdrawal and BMP4 treatment; 2 days of BMP4 treatment which included 2 days of proliferation to yield 60%–70% confluency and 2 days of EGF withdrawal and BMP4 treatment; 3 days of BMP4 treatment which included 1 day of proliferation to yield 60%–70% confluency and 3 days of EGF withdrawal and BMP4 treatment. Cells cultured for 4 days in the presence of growth factors was used as the proliferation control for the BMP4 experiment. To recover cells into proliferation following BMP4 treatment, cells were split and re-plated in the presence of growth factors. Cells were given 1, 2 or 3 days to recover and proliferate. This plating scheme enabled the ROS profiling of cells in different states on the same day, which enabled us to avoid day-to-day fluctuations in cytometric readouts. Two different experiments were conducted at the end of each of the above treatments. First, ROS dyes were added to cells 30 min prior to addition of accutase (similar concentrations as described above for *in vivo* ROS profiling), cells were washed, subjected to centrifugation, resuspended in PBS and the cellular ROS content was analyzed using the LSR2 cell analyzer (BD Biosciences). Second, to assay proliferation a Click-IT assay was performed, which involved labeling proliferating cells with 3-hour exposure to EdU. Following the EdU-labeling, cells were accutased, fixed with 4% PFA, the Click-IT reaction was performed as per manufacturer's protocol (Thermo Fischer EdU Click-IT cytometric assay kit) and cells were cytometrically analyzed.

ROS profiling of *in vivo* proliferating cells

To label proliferating cells, animals were injected intraperitoneally with EdU (50 mg/kg). 2 h after the last injection animals were either sacrificed (Acute-EdU) or housed for 2 additional days (delayed-EdU). Following sacrifice, DG were isolated as

described above and stained for ROS content and vitality as described above. After staining, the cells were spun down, fixed with 4%PFA and EdU was detected as per manufacturer's protocol and cells were cytometrically analyzed for GFP, ROS and EdU content.

Next Generation sequencing

RNA extraction and sequencing

Two separate RNA sequencing experiments were performed in this study. In the first experiment, tissue was microdissected from the SVZ and the DG of the same standard housed animals following the protocol of Walker and Kempermann (2014). RNA was extracted using the RNeasy micro kit (QIAGEN). In the second experiment, Nes-GFP positive cells from the DG from 6-8-week-old standard housed animals were gated into ROS classes, based on their cellular ROS content. 400 GFP positive cells from each ROS class were sorted into a PCR tube containing 8.5 μL of a hypotonic reaction buffer and RNA was prepared using the SMARTer Ultra Low RNA HV Kit (Takara Bio) according to the manufacturer's protocol. For both experiments, cDNA of polyadenylated mRNA was synthesized from RNA of the lysed cells using SmartScribe reverse transcriptase, a universally tailed poly-dT primer and a template switching oligonucleotide (Takara Bio). This was followed by 12 cycles of amplification of the purified cDNA with the Advantage 2 DNA Polymerase (Takara Bio). After ultrasonic shearing of the amplified cDNA (Covaris S2), samples were subjected to standard Illumina fragment library preparation using the NEBnext Ultra DNA library preparation chemistry (New England Biolabs). In brief, after physical fragmentation by ultrasonication (Covaris LE 220) cDNA fragments were end-repaired, A-tailed and ligated to indexed Illumina Truseq adapters. Resulting libraries were PCR-amplified for 15 cycles using universal primers, purified using XP beads (Beckman Coulter) and then quantified with the Fragment Analyzer (Advanced Analytics/Agilent). Final libraries were equimolarly pooled and subjected to 75 bp single-end sequencing on the Illumina HiSeq2500 platform, providing ~35 (24–60) million reads per sample. Reads were mapped to the latest mouse genome build (mm10) using the STAR algorithm (Dobin et al., 2013) and counts per ENSEMBL gene model prepared using the *RSubread* package (Liao et al., 2013) in R/BioConductor.

Quality control and differential expression

RNASeq counts were filtered to have at least 1 count per million reads (CPM) in a minimum of 75% of the samples from at least one cell population. CPM were calculated using the function *cpm* from the *edgeR* package in R/BioConductor (Robinson et al., 2010). Samples were clustered by plotting the first two principal components and by unsupervised hierarchical clustering. One sample from each of the two experiments showed reduced sequencing depth and complexity and did not cluster with replicates. In both cases, these samples came from preparations with very low input RNA so we decided to remove them from further analyses. A filter for differential expression was then performed using the *edgeR* functions *lmFit* and *topTags* and only significantly (adjusted $p < 0.05$) differentially expressed transcripts were used for enrichment analyses. Transcripts were classified as 'enriched' in an experimental group if the mean expression in that group was significantly above the average expression over all groups. Enriched genes were further filtered by hierarchical clustering into two clusters based on inter-group *t*-statistics and those where only one group clustered separately were termed 'signature' genes (for the DG/SVZ comparison, these are obviously equivalent to the 'enriched' gene set).

Functional enrichment and expression profiles

Enrichment for Gene Ontology terms was performed using the R package *topGO* (Alexa and Rahnenfuhrer, 2018) with the DG/SVZ 'enriched' gene lists as query sets and all genes passing the CPM filter (see above) as background. Expression profiles of curated gene lists were calculated by identifying all genes in the current data that corresponded to the genes in the gene list of interest and calculating the first principal component to collapse their expression into an 'eigengene'. The eigengene values were then used for plotting. A similar approach was used to reanalyze the Shin et al. dataset where the genes corresponding to the 'signature' genes for each ROS class were identified in the single-cell dataset and the first principal component of these used to create an eigengene. Smooth spline interpolation of the eigengene was then performed to produce the plotted values.

RNA isolation and quantitative RTPCR (q-RTPCR)

DG of the Dcx-GFP animals were micro-dissected and cells were sorted into RLT buffer. Total RNA was isolated from sorted cells using the RNeasy Micro Kit (QIAGEN) according to the manufacturer's instructions. RNA was eluted at least four times from RNeasy columns and the volume reduced to 10 μL using a Speedvac (Eppendorf) at 37°C. RNA was reverse transcribed into complementary DNA (cDNA) using SuperScript™ II Reverse Transcriptase (Thermo Fisher Scientific). Briefly, 0.5 - 1 μg of RNA was incubated with 500 ng Oligo(dT) primers and 1 μL dNTPs (10 mM; Thermo Fisher Scientific) for 5 min at 65°C and quickly chilled on ice. For cDNA amplification, RNaseOut (Thermo Fisher Scientific) was added and incubated at 40°C for 2 h.

Quantitative real-time polymerase chain reactions (qRT-PCRs) were performed using the QuantiFast SYBR Green PCR Kit (-QIAGEN) and the CFX Connect™ Real-Time PCR Detection System (Bio-Rad). Briefly, 20 μL reactions consisting of 10 μL SYBR Mix, 2 μL primers (10 mM) and 8 μL of undiluted cDNA were incubated using the PCR program. Primer specificity was further ensured by validating single peak melting curves. Results of qRT-PCRs were analyzed using the delta Ct method. For normalization, gene-

specific Ct values were subtracted from Ct values obtained for the housekeeping gene, beta-Actin (*Actb*). Thermal cycling conditions for qrt-PCRs (denaturation to extension were repeated for 40 cycles).

Cycling conditions for q-RTPCRs

Step	Temperature	Time
Initial denaturation	95°C	15 min
Denaturation	95°C	10 s
Annealing	59°C (see materials)	30 s
Extension	72°C	30 s
Final extension	72°C	10 min
Melting curve	Ramp down from 95°C to 60°C	

Ki67 immunohistochemistry and quantification of *in vivo* proliferation

Briefly, brain sections stored in CPS were transferred into PBS and washed. Endogenous peroxidase activity was blocked by adding 0.6% hydrogen peroxide (H_2O_2; Merck Millipore) for 30 min and sections were then rinsed with 0.9% NaCl. Protein-binding sites were blocked with a blocking solution (10% donkey serum, 0.2% Triton X-100 in PBS) for 1 h. Ki67 staining was performed with the Ki67 primary (rabbit anti-Ki67, 1:500; Novocastra) and donkey anti-rabbit-biotin secondary antibodies (1:1000; Jackson Immunoresearch Laboratories). Detection was performed using the Vectastain ABC-Elite reagent (Vector Laboratories) with diaminobenzidine (Sigma-Aldrich) and 0.04% NiCl as the chromogen. Sections were mounted onto gelatin-coated glass slides, dried, cleared with Neoclear (Merck) and coverslipped using Neo-mount (Merck). Every sixth section (240 μm apart) was counted in the complete ventral dorsal extent of the dentate gyrus, at 40x magnification using a standard brightfield microscope. Results were multiplied by 6 in order to obtain the total number of positive cells within the DG region of each brain.

Protein electrophoresis and western blot analysis

Animals were housed with/without running wheels for 1-4 days. Following the stimulus, animals were sacrificed, DG were isolated, homogenized and incubated on ice for 30 min in buffer containing 50 mM Tris pH = 7.5, 150 mM NaCl, 2.5 mM MgCl2, 1% Triton X-100, 5% Glycerol and 100 mM 2-Iodoacetamide, supplemented with EDTA-free Protease inhibitor cocktail and PhosSTOP phosphatase inhibitor, followed by clearance of lysates at > 18000 g for 15 min. Lysates were either subjected to immunoprecipitation with mouse monoclonal anti-PTEN antibody for 2h at 4°C or directly used for Western Blot analysis. The proteins were denatured using NuPAGE LDS buffer and 100 mM DTT was added to half of the samples. The proteins were resolved on a non-reducing SDS-PAGE and revealed by western blotting using quantitative infrared scanning system (Odyssey, LICOR, Lincoln, Nebrasca, USA) with rabbit monoclonal anti-PTEN antibody. To quantify total Akt (pan) and phospho- Akt (Ser473; Thr308) samples were loaded on a non-reducing SDS-PAGE and revealed by western blotting using quantitative infrared scanning system with mouse monoclonal anti-β-Actin as a loading control. All blots were analyzed using Imagestudio (LICOR, Lincoln, Nebrasca, USA). Oxidized PTEN was normalized to total PTEN levels and for Akt/p-Akt, signal was normalized first to loading control followed by relative determination (p-Akt relative to pan-Akt).

QUANTIFICATION AND STATISTICAL ANALYSIS

Data analysis (with the exception of the next-generation sequencing data) was performed using Prism software (Version 8, GraphPad Software, Inc). Flow cytometry data was analyzed using the FlowJo software. Results were expressed as mean ± standard error of the mean (SEM). Statistical significance was determined using a Student's t test when the experiment contained two groups, an ANOVA when comparing more than two groups, or a one-sample t test when comparing to a hypothetical value. Dunnett, Tukey's and Sidak post hoc tests were performed and mentioned in the text wherever applicable. The level of conventional statistical significance was set at $p < 0.05$ and displayed visually as * $p < 0.05$, ** $p < 0.01$, and *** $p < 0.001$. The number of mice or repeat experiments performed per group is stated in Table S5.